

Cite this: *Nanoscale*, 2022, 14, 15560

# Alloying strategies for tuning product selectivity during electrochemical CO<sub>2</sub> reduction over Cu

Venkata Sai Sriram Mosali,<sup>a</sup> Alan M. Bond <sup>a,b</sup> and Jie Zhang <sup>\*a,b</sup>

Excessive reliance on fossil fuels has led to the release and accumulation of large quantities of CO<sub>2</sub> into the atmosphere which has raised serious concerns related to environmental pollution and global warming. One way to mitigate this problem is to electrochemically recycle CO<sub>2</sub> to value-added chemicals or fuels using electricity from renewable energy sources. Cu is the only metallic electrocatalyst that has been shown to produce a wide range of industrially important chemicals at appreciable rates. However, low product selectivity is a fundamental issue limiting commercial applications of electrochemical CO<sub>2</sub> reduction over Cu catalysts. Combining copper with other metals that actively contribute to the electrochemical CO<sub>2</sub> reduction reaction process can selectively facilitate generation of desirable products. Alloying Cu can alter surface binding strength through electronic and geometric effects, enhancing the availability of surface confined carbon species, and stabilising key reduction intermediates. As a result, significant research has been undertaken to design and fabricate copper-based alloy catalysts with structures that can enhance the selectivity of targeted products. In this article, progress with use of alloying strategies for development of Cu-alloy catalysts are reviewed. Challenges in achieving high selectivity and possible future directions for development of new copper-based alloy catalysts are considered.

Received 28th June 2022,  
Accepted 5th October 2022

DOI: 10.1039/d2nr03539a

rsc.li/nanoscale

## 1. Introduction

Carbon dioxide (CO<sub>2</sub>) is a greenhouse gas that is a major contributor to global warming. In recent years, the concentration of CO<sub>2</sub> in the atmosphere has increased rapidly, resulting in the rise of global temperatures, which disturbs the ecological balance. In nature, the CO<sub>2</sub> released into the atmosphere by natural processes is utilised by terrestrial plants and aquatic species, thus achieving a carbon balance. However, excessive dependency on fossil fuels in the modern chemical industry, particularly the automobile and electricity generation sectors, has led to the accumulation of additional CO<sub>2</sub> in the atmosphere.<sup>1</sup> In a recent report, the National Oceanic and Atmospheric Administration (NOAA) global monitoring laboratory advised of a 2.3 ppm surge in CO<sub>2</sub> levels in 2020 to 2021 period leading to an average level of 419 ppm in 2021.<sup>2</sup> Fig. 1 shows the global monthly mean CO<sub>2</sub> emissions in the atmosphere from 1980 until May 2022 reported by NOAA which reveal the seriousness of the carbon accumulation problem. However, if an effective CO<sub>2</sub> capture, storage and conversion to chemical fuels technologies can be developed, the CO<sub>2</sub> can be recycled. Ideally, if CO<sub>2</sub> is sourced directly through air or bio-

energy carbon capture and storage and reacted with renewable H<sub>2</sub>, the carbon cycle can be closed.<sup>3</sup>

A range of methods such as photochemical,<sup>4–7</sup> biochemical,<sup>8–10</sup> and photo-/thermochemical,<sup>11–15</sup> have been explored for conversion of CO<sub>2</sub> to value added chemicals or fuels. However, their success is highly sensitive to the reaction environment.<sup>16</sup> Another possibility is use of the electrochemical CO<sub>2</sub> reduction reaction (eCO<sub>2</sub>RR) which can be per-

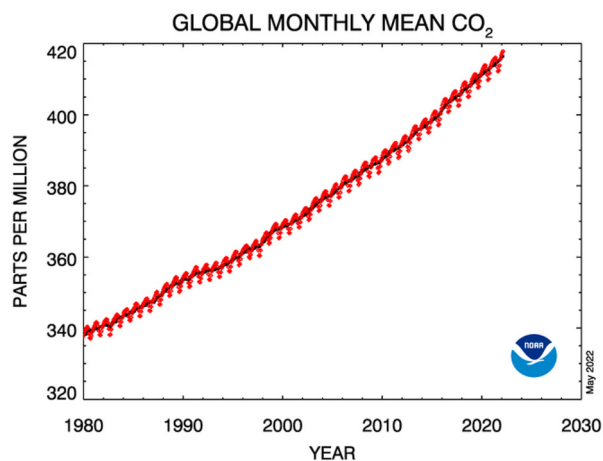


Fig. 1 Monthly mean CO<sub>2</sub> emissions from 1980 to May 2022 as reported by the NOAA global monitoring laboratory.<sup>2</sup>

<sup>a</sup>School of Chemistry, Monash University, Clayton 3800, Victoria, Australia.

E-mail: jie.zhang@monash.edu

<sup>b</sup>ARC Centre of Excellence for Electromaterials Science, Monash University, Clayton 3800, Victoria, Australia

formed under ambient conditions using non-toxic materials and electrical energy from renewable sources, making it a highly desirable approach.<sup>17</sup>

The eCO<sub>2</sub>RR can be performed in aqueous and non-aqueous media where the former are attractive in terms of non-toxicity, low cost, good conductivity, high proton availability and eco-friendliness. Aqueous electrolytes used are generally alkali salts comprising Na<sup>+</sup>, K<sup>+</sup>, Li<sup>+</sup>, Rb<sup>+</sup>, or Cs<sup>+</sup> cations and OH<sup>-</sup>, HCO<sub>3</sub><sup>-</sup>, Cl<sup>-</sup>, H<sub>2</sub>PO<sub>4</sub><sup>-</sup> or SO<sub>4</sub><sup>2-</sup> anions. Both cations and anions can have a strong impact on the efficiency of eCO<sub>2</sub>RR as well as product selectivity.<sup>18–21</sup> Additionally, other factors, such as temperature and pH (more critically local pH, since it can differ substantially from the bulk value, especially under high current density/low buffer capacity conditions) also influence the product selectivity during the eCO<sub>2</sub>RR.<sup>22–24</sup> Table 1 provides several examples of eCO<sub>2</sub>RR products generated in aqueous media and their reversible potentials (*E*<sup>o</sup>) vs. the reversible hydrogen electrode (RHE). Significant drawbacks of eCO<sub>2</sub>RR in aqueous solutions are the low solubility of CO<sub>2</sub> resulting in low current densities, the presence of a competitive hydrogen evolution reaction (HER) which suppresses the overall eCO<sub>2</sub>RR efficiency, in addition to sluggish kinetics and hence a large overpotential required to produce commercially desirable products at a sufficient rate.<sup>17,21,25</sup>

To date, three types of electrolyzers have been mainly used for the eCO<sub>2</sub>RR. The H-cell is most commonly used since it is easy to construct and facilitates rapid screening of catalysts and electrolyte composition. Fig. 2(a) shows a conventional H-cell for eCO<sub>2</sub>RR. In this, the aqueous electrolytes used in most cases in both anodic and cathodic compartments are pre-saturated with CO<sub>2</sub>. The cell is then sealed prior to performing electrolysis allowing gaseous products to be collected and quantified. The solubility of molecular CO<sub>2</sub> in these electrolytes is around 30 mM at 1 bar and thus the rate of CO<sub>2</sub> reduction is limited with a current density of typically less than 100 mA cm<sup>-2</sup>.<sup>26</sup> To overcome the drawback of the low mass transport rate associated with the H-cell, electrolyzers equipped with a gas diffusion electrode (GDE) have been developed. In these electrolyzers, the CO<sub>2</sub> gas is diffused through a thin electrolyte layer on the GDE, with the diffusion length being ~50 nm.<sup>27</sup> The much higher mass transport rate

**Table 1** Electrochemical reactions relevant to eCO<sub>2</sub>RR and their reversible potentials.<sup>17</sup>

| Half-cell reaction   | <i>E</i> <sup>o</sup> (V vs. RHE) |
|--|-----------------------------------|
| CO <sub>2</sub> + 2H <sup>+</sup> + 2e <sup>-</sup> → HCOOH(aq)  | -0.12                             |
| CO <sub>2</sub> + 2H <sup>+</sup> + 2e <sup>-</sup> → CO(g) + H <sub>2</sub> O                                     | -0.10                             |
| CO <sub>2</sub> + 6H <sup>+</sup> + 6e <sup>-</sup> → CH <sub>3</sub> OH(aq) + H <sub>2</sub> O                    | 0.03                              |
| CO <sub>2</sub> + 8H <sup>+</sup> + 8e <sup>-</sup> → CH <sub>4</sub> (g) + 2H <sub>2</sub> O                      | 0.17                              |
| 2CO <sub>2</sub> + 8H <sup>+</sup> + 8e <sup>-</sup> → CH <sub>3</sub> COOH(aq) + 2H <sub>2</sub> O                | 0.11                              |
| 2CO <sub>2</sub> + 10H <sup>+</sup> + 10e <sup>-</sup> → CH <sub>3</sub> CHO(aq) + 3H <sub>2</sub> O               | 0.06                              |
| 2CO <sub>2</sub> + 12H <sup>+</sup> + 12e <sup>-</sup> → C <sub>2</sub> H <sub>4</sub> (g) + 4H <sub>2</sub> O     | 0.08                              |
| 2CO <sub>2</sub> + 12H <sup>+</sup> + 12e <sup>-</sup> → C <sub>2</sub> H <sub>5</sub> OH(aq) + 3H <sub>2</sub> O  | 0.09                              |
| 2CO <sub>2</sub> + 14H <sup>+</sup> + 14e <sup>-</sup> → C <sub>2</sub> H <sub>6</sub> (g) + 4H <sub>2</sub> O     | 0.14                              |
| 3CO <sub>2</sub> + 16H <sup>+</sup> + 16e <sup>-</sup> → C <sub>2</sub> H <sub>5</sub> CHO(aq) + 5H <sub>2</sub> O | 0.09                              |
| 3CO <sub>2</sub> + 18H <sup>+</sup> + 18e <sup>-</sup> → C <sub>3</sub> H <sub>7</sub> OH(aq) + 5H <sub>2</sub> O  | 0.10                              |

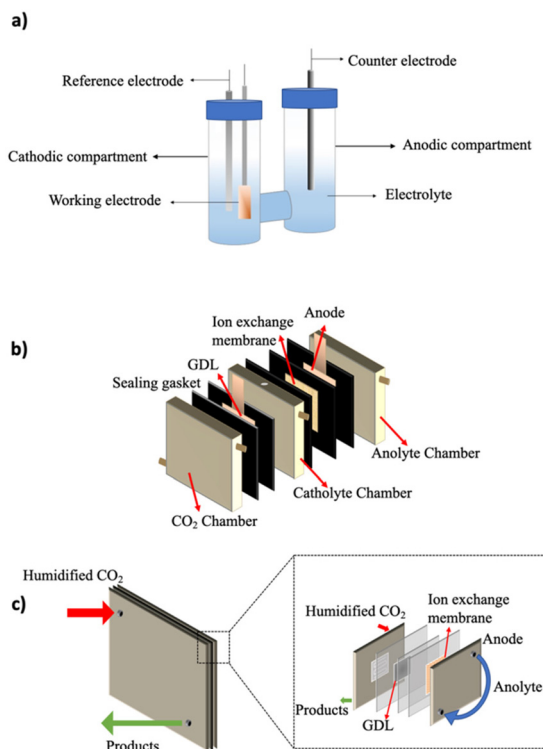


**Fig. 2** Illustration of (a) H-cell, (b) flow cell and (c) zero gap MEA electrolyzers used for eCO<sub>2</sub>RR.

achieved under these conditions allows an industrially appropriate current density of above 0.5 A cm<sup>-2</sup> to be achieved.<sup>27–29</sup> Two types of such electrolyzers are commonly used; the flow-cell and membrane electrode assembly (also known as zero-gap) electrolyzers. To fabricate a GDE, a gas diffusion layer (GDL) is coated with a layer of catalyst. GDLs composed of carbon fibers possess high porosity.<sup>30,31</sup> The structure of the GDE has an impact on the transport of both reactants and products, which affects chemical species adsorption and depletion at the catalyst surface, and hence the overall eCO<sub>2</sub>RR performance.<sup>31,32</sup>

Properties such as porosity, electrical conductivity and hydrophobicity of the GDLs are now being tailored to improve the cell performance.<sup>30</sup> A typical flow-cell electrolyzer is shown in Fig. 2(b) and consists of three channels, one for the CO<sub>2</sub> gas flow and the other two for electrolyte (catholyte and anolyte). The GDE is placed in between the CO<sub>2</sub> gas and catholyte channels. The catholyte and anolyte are separated by a polymer exchange membrane (PEM). The PEM used in the cell also greatly impacts the efficiency of the electrolyzer. Cation exchange membranes (CEM) and anion exchange membranes (AEM) are the two types of PEM used depending on the reaction environment. Nafion, a CEM, was explored for eCO<sub>2</sub>RR by Delacourt *et al.*<sup>33</sup> and found to suffer from excessive H<sub>2</sub> production and lack of stability in long-term electrolysis. AEMs are better suited for eCO<sub>2</sub>RR circumstances because neutral or alkaline media can be used to minimize the competing H<sub>2</sub> evolution reaction. Since anions are far less mobile than

protons, both in solution and in the membrane, an additional driving force (*i.e.* larger overpotential) is needed to overcome the resistance effect. Further, the transport of bicarbonate ions away from the cathode also diminishes the eCO<sub>2</sub>RR performance.<sup>30,34,35</sup> The ratio of CO<sub>2</sub> and the proton source in a flow cell electrolyser is significantly higher than that found in an H-cell electrolyser. Furthermore, during the eCO<sub>2</sub>RR, CO<sub>2</sub> is reduced and protons are consumed. Hence, the local reaction environment under the flow-cell conditions may be drastically different from that found under H-cell conditions due to its inherently higher CO<sub>2</sub> mass transport rate and hence higher current density. Accordingly, the results obtained with an H-cell may not be applicable under flow-cell conditions. Consequently, eCO<sub>2</sub>RR performance ideally should be assessed under commercially relevant conditions using a flow cell-electrolyser. H-cell and flow-cell electrolysers are mainly used for fundamental research. The presence of a reference electrode in these configurations allows the anode and cathode to be investigated separately. In commercial applications, a reference electrode is not needed. A membrane electrode assembly (MEA) electrolyser is commonly used, inspired by developments of fuel cells, a closely related research area. A MEA electrolyser is composed of two channels, one for CO<sub>2</sub> and the other for anolyte (Fig. 2c). The PEM is sandwiched between the anode and the cathode to minimize the cell resistance. Use of a MEA electrolyser allows the full cell performance, including energy efficiency, to be evaluated.

The catalyst employed in an eCO<sub>2</sub>RR is critical in determining the eCO<sub>2</sub>RR product selectivity.<sup>36</sup> During electrolysis, the CO<sub>2</sub> molecule commonly is adsorbed onto the catalyst present in the cathode. Accordingly, the CO<sub>2</sub> reduction pathway usually depends on the binding strength of CO<sub>2</sub> and its reduced intermediates over the catalyst surface, as depicted in Fig. 3 and 4. CO<sub>2</sub> adsorbed on the catalyst is initially reduced to either carbonyl (\*COOH) (an asterisk is used to indicate an adsorbed species) or formyl (\*OCHO) intermediates in aqueous electrolyte which can be further reduced to CO and formate, respectively. CO is electroactive. However, if CO binds

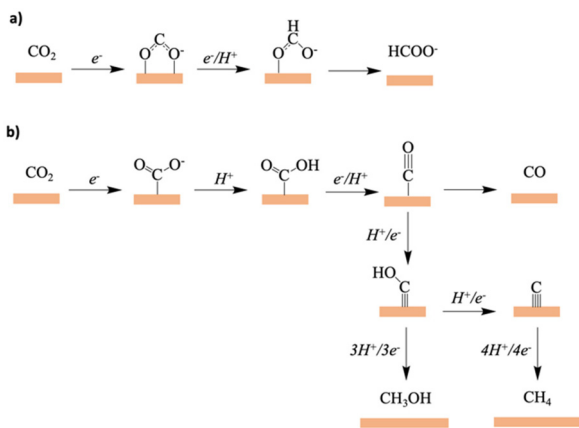


Fig. 3 Illustration of eCO<sub>2</sub>RR pathways for the formation of (a) HCOO<sup>-</sup>, (b) CO, CH<sub>3</sub>OH, CH<sub>4</sub>.

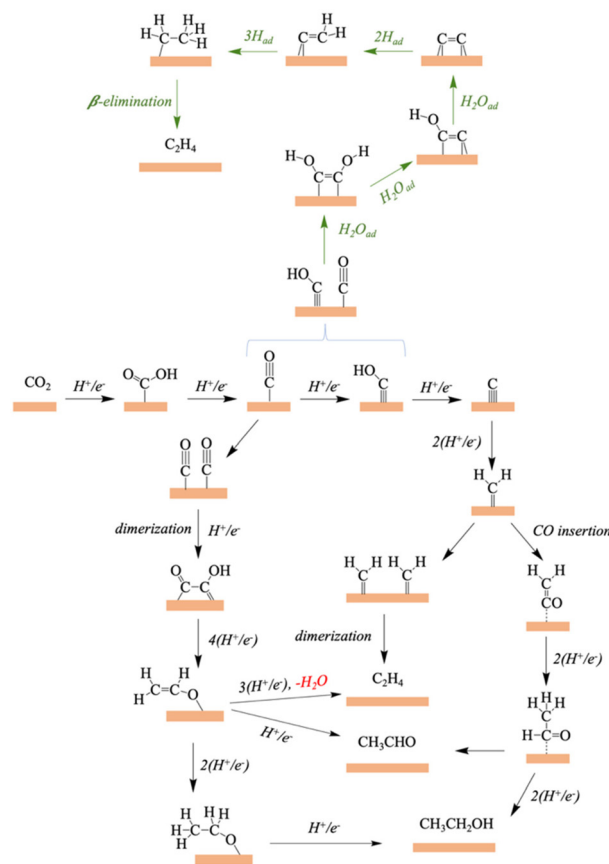


Fig. 4 Illustration of eCO<sub>2</sub>RR pathways for the formation of C<sub>2</sub>H<sub>4</sub>, CH<sub>3</sub>CHO and C<sub>2</sub>H<sub>5</sub>OH.

to the catalyst too strongly, then further reduction to desirable products and their subsequent desorption is inhibited. Poisoning of the catalyst also is likely to occur. Consequently, hydrogen evolution rather than CO<sub>2</sub> reduction may become the favoured reduction pathway. This scenario occurs at Pt, Ni, and Fe electrodes.<sup>37</sup> Alternatively, if the \*CO binding ability to the catalyst is weak, as applies with metals such as Zn, Au, and Ag, then high selectivity for CO as the product is achieved.<sup>37</sup> If the catalyst has moderate binding strength for \*CO, further reduction is facilitated, leading to more reduced carbon products. Cu is the only catalyst that has moderate \*CO binding energy, leading to unique prospects for formation of a wide range of products. Metals which bind eCO<sub>2</sub>RR intermediates too weakly are also likely to bind \*H weakly. If these catalysts also possess strong \*O affinity, an O-bound \*OCHO intermediate will be formed during the initial reaction step which leads to formation of HCOOH.

As noted above, extensive eCO<sub>2</sub>RR studies with many metals in the periodic table have revealed that Cu has the unique capability of producing an extensive range of reduced carbon products containing one carbon (C<sub>1</sub>), two carbons (C<sub>2</sub>) or multi-carbons (*i.e.* more than two carbons; C<sub>2+</sub>). The 16 products detected using Cu catalysts during eCO<sub>2</sub>RR and their structures are shown in Fig. 5.<sup>38–41</sup> This on one hand demon-

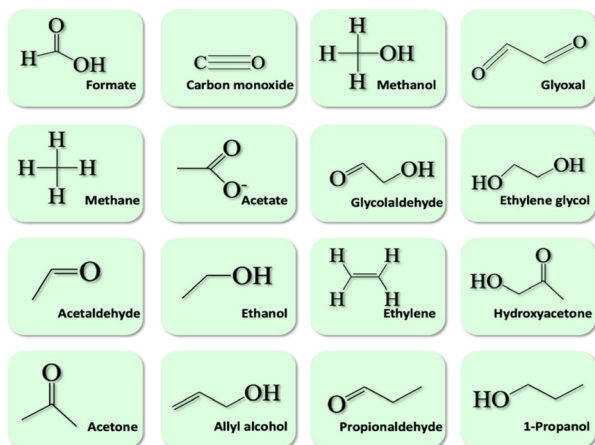


Fig. 5 Graphical representation of products detected during eCO<sub>2</sub>RR at a Cu electrode. Adopted and redrawn.<sup>38</sup>

strates the versatility of Cu catalysts, but on the other hand implies that poor product selectivity is a major challenge to address for commercial applications.

In attempts to address the selectivity issue, nanostructuring, alloying, defect engineering, atomizing, and the synthesis of oxide, sulphide, and nitride-derived Cu as well as other methods have been employed.<sup>17,21,42–49</sup>

Since alloying is one of the most promising and fundamental strategies for manipulating the reaction pathways to obtain desired products, this review focuses on what has been achieved to date and what might be accomplished in the future by alloying Cu with other eCO<sub>2</sub>RR active metals. Several review articles<sup>17,25,50–54</sup> have been published on the use of alloyed-Cu catalysts. However, they focus on a much broader aspect of eCO<sub>2</sub>RR with copper. In this review, the correlation between alloy type and selectivity is examined and future directions in the development of Cu based alloys as effective eCO<sub>2</sub>RR catalysts are proposed. Finally, in order to provide an overview of the status of findings with alloyed-Cu catalysts, comparisons of what has been achieved with state-of-the-art Cu alloys and other Cu based catalysts for each eCO<sub>2</sub>RR product also are provided in a table at the end of each section.

## 2. Catalyst performance descriptors

The effectiveness of eCO<sub>2</sub>RR is determined by the following descriptors:

(a) Faradaic efficiency: faradaic efficiency (FE) is the indicator of the selectivity of the products obtained with a catalyst during eCO<sub>2</sub>RR. FE (reported in %) is calculated by using the formula given in eqn (1)

$$\text{FE (\%)} = \frac{nNF}{Q} \times 100 \quad (1)$$

where  $N$  represents the number of moles of the product formed,  $n$  is the number of electrons transferred for the formation of one molecule of the product,  $F$  is the Faraday con-

stant ( $96485 \text{ C mol}^{-1}$ ) and  $Q$  is the amount of charge passed during electrolysis.

(b) Overpotential: overpotential ( $\eta$ ) is the difference between the applied potential ( $E_{\text{applied}}$ ) to obtain a product and the equilibrium potential ( $E^{\circ}$ ). It is calculated by using the formula given in eqn (2)

$$\eta = |E_{\text{applied}} - E^{\circ}|. \quad (2)$$

(c) Current density: current density ( $j$ ) denotes the rate/s of electrochemical reaction/s. It is the catalytic current ( $i$ ) generated per unit area. Current densities presented in many studies are calculated with respect to the geometric area of the electrode. However, ideally an electrochemical active surface area should be used. Partial current density ( $j_{\text{product}}$ ) indicates the rate of formation of a given product and calculated by the formulae given in eqn (3) and (4)

$$j_{\text{total}} = \frac{i_{\text{total}}(\text{mA})}{\text{area}(\text{cm}^2)} \quad (3)$$

$$j_{\text{product}} = j_{\text{total}} \times \text{FE}_{\text{product}} \quad (4)$$

(d) Stability: the stability is the lifetime of a catalyst for performing eCO<sub>2</sub>RR. In general, it is the time period for which a catalyst provides stable activity and selectivity.

## 3. Strategies for alloying copper

Watanabe *et al.*,<sup>55</sup> were the first to report eCO<sub>2</sub>RR on Cu alloys formed by electroplating. They found that alloy catalysts often exhibited distinctly different catalytic properties from their constituent elemental metals. This feature was later attributed to electronic and geometric effects at the catalyst surface that arise due to alloying.<sup>17,36,50,56</sup> The electronic effect is generated in an alloy due to the interaction between the constituent elemental metals with different electronic properties and/or the lattice mismatch between two adjacent metals, which alters the binding strength of the eCO<sub>2</sub>RR intermediates. The geometric effect arises from the change in the arrangement of the alloyed metals in the catalyst which alters the environment near the active sites for the eCO<sub>2</sub>RR intermediates and hence impacts their binding and subsequent reactions.

The structure of the alloy or in other words, its atomic arrangement play a crucial role in determining the selectivity of the products formed during eCO<sub>2</sub>RR. Alloy systems can be ordered, intermetallic, disordered, core/shell structured, phase-separated and have high entropy structures (Fig. 6(a)). All these variations have been explored in the design of catalysts for eCO<sub>2</sub>RR. Intermetallic alloy systems having an ordered atomic arrangement are the most stable form of alloys. With thermodynamically stable alloy forms, the electronic structure and atomic co-ordination environment can be controlled precisely as they possess a specific crystal structure.<sup>57</sup> By altering the alloy composition, bond lengths can be tuned, which effects the binding energies of molecules adsorbed on the surface of the catalysts and hence their catalytic behaviour.

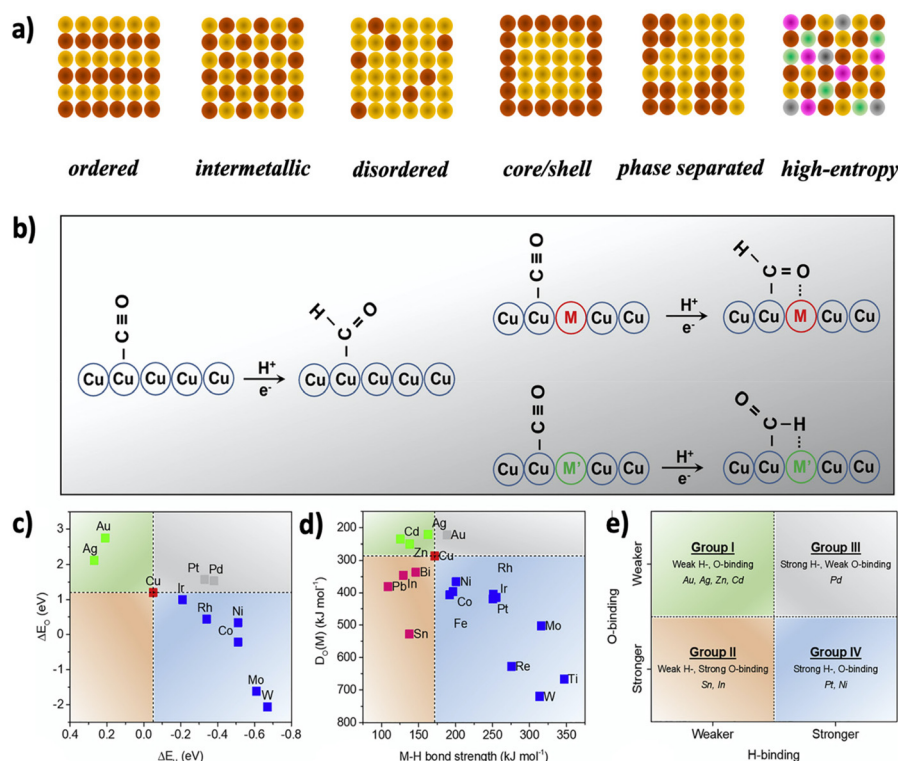


**Fig. 6** (a) Alloy systems reported in the literature. (b) Illustration of binding of eCO<sub>2</sub>RR intermediates to Cu, Cu–M and Cu–M' alloy catalysts where M is the guest metal with O-affinity and M' is the guest metal with H-affinity, (c) H and O binding energies for designated metals, (d) M–H bond strength shown as a function of bond dissociation enthalpy of metal oxides, (e) classification of metals into different groups with respect to Cu, based on their O and H affinities. Reprinted with permission.<sup>25</sup> Copyright 2018, Elsevier Inc.

Disordered alloys are solid-solution mixtures with irregular arrangements of binary atoms. They are generally thermodynamically unstable and their local electronic and the geometry of their structures often changes during the electrolysis process.<sup>57,58</sup>

The catalytic properties in core/shell structured alloys are regulated by the strain and ligand effects that arise between the core and shell materials. Strain effects such as tensile stress on the surface of atoms arise due to the lattice mismatch between core/shell interface.<sup>59,60</sup> Ligand effects are short-range and only exist within two or three atomic layers from the surface.<sup>61</sup> Atomic vacancies and metal doping in the shell material also can occur. They are a function of the thickness of the shell and also impact on the product selectivity during electrolysis.<sup>62</sup> In eCO<sub>2</sub>RR, the major benefit of such alloys is the creation of phase interfaces where the products formed at one phase can migrate through the interface and be further reduced to C<sub>2+</sub> products. These catalytic Cu alloy forms are being extensively studied as a means of increasing the CO environment at Cu and facilitating the production of highly reduced C<sub>2+</sub> products such as ethylene and ethanol.<sup>63–65</sup> Details of the efficiency of phase separated alloy catalysts and the CO spill-over effect are discussed below.

High entropy alloys (HEAs) are a novel class of alloys recently being investigated for eCO<sub>2</sub>RR. These alloys are formed by about five metals, with each element constituting

between 5–35% and with variation in the elemental ratios. Accordingly, a large variety of elemental combinations is possible in the alloy and consequently a wide range of catalytic capabilities can be achieved.<sup>66,67</sup>

Compared to bimetallic alloys, HEAs provide superior stability and durability particularly under harsh reaction conditions such as high temperature and high electrochemical potential due to their high mixing entropy and hence low Gibbs free energy as quantified by eqn (5).<sup>67,68</sup>

$$\Delta G_{\text{mix}} = \Delta H_{\text{mix}} - T\Delta S_{\text{mix}} \quad (5)$$

where  $\Delta G_{\text{mix}}$  is the change in the Gibbs free energy of the alloy system,  $\Delta S_{\text{mix}}$  is the change in the entropy of the alloy system,  $\Delta H_{\text{mix}}$  is the change in the enthalpy of the alloy system, and  $T$  is the temperature. In addition, the random atomic arrangement in the lattice leads to variation in lattice potential energy at different locations which provides a higher diffusion activation energy that contributes to the stability of the alloy.<sup>69</sup> Furthermore, due to lattice distortion effects resulting from the presence of multiple elements, HEAs have more flexibility to alter their chemical and physical properties.<sup>67,70,71</sup> In terms of electrolysis, this effect helps the optimization of the coordination environment of atoms on the catalyst surface as well as the adsorption and desorption energies of key reaction intermediates.<sup>68</sup> Similar to the synergistic effects in bimetallic

alloys, HEAs possess a “cocktail effect” resulting from the interactions between multiple elements. As a result of a range of novel features, these alloys offer new properties with respect to corrosion and oxidation resistance, and other mechanical properties.<sup>68,70</sup> The unique characteristics of HEAs change the scaling relationships and provide a wide window of opportunity for manipulating the reaction pathways and overcoming the limitations of conventional alloys.<sup>72</sup>

Grouping of metals according to their binding affinities for \*H and \*O relative to copper was proposed to facilitate the selection of a guest metal to form a binary alloy with Cu.<sup>25</sup> In the alloy, the bimetallic catalyst material will have two binding sites available to achieve stabilisation of a desired intermediate. For example, metals which produce hydrogen have a more robust \*H and \*O affinity than Cu while those with weaker \*O and \*H binding strengths, produce CO *via* a \*COOH intermediate. Metals having a lower H affinity but higher O-affinity than Cu favour formation of the \*OCHO intermediate, which leads to formation of formate. Hence, metals with good O-affinity can be alloyed with Cu to stabilize O-bound intermediates, while those having H-affinity can stabilize H binding in the intermediates, as illustrated in Fig. 6(b). Fig. 6(c–e) show a comparison of O and H affinities of some metals with respect to copper and the grouping of metals. In the following sections, the factors that govern the selectivity of Cu alloy towards each product are summarized and discussed to guide the development of advanced alloy catalysts. Examples of the state-of-the-art Cu alloys and other Cu based catalysts for each product are also given.

## 4. Copper alloys for selective reduction of CO<sub>2</sub>

### 4.1 Formate and CO

**4.1.1 Formate.** Catalysts obtained by alloying Cu with formate favouring metals, such as Bi,<sup>74–78</sup> Sn,<sup>79–83</sup> Pb,<sup>84–88</sup> Pd,<sup>89–93</sup> Mo<sup>94</sup> and Sb,<sup>95–97</sup> particularly as intermetallics, composites and surface alloys, often produces formate with good efficiency.<sup>98,99</sup>

Copper modified with Pd and Pd–H produces significant amounts of formate. For example, early studies by Fujishima and co-workers showed substantial formate production at the Pd modified Cu electrodes.<sup>100,101</sup> Zhang *et al.*<sup>102</sup> have synthesised a stannate derived Sn–Cu bimetallic catalyst *via* cation exchange with Na<sub>2</sub>Sn(OH)<sub>6</sub> followed by annealing and electroreduction. This Cu–Sn catalyst produced 86% formate at –1.1 V *vs.* RHE in 0.5 M NaHCO<sub>3</sub> with a partial current density of ~11 mA cm<sup>–2</sup>. These authors also reported that a slight increase in formate faradaic efficiency could be achieved by incorporating the Cu–Sn catalyst into reduced graphene oxide along with a major increase in partial current density. The Hod group<sup>103</sup> reported the favorable formation of formate with 3D structured Cu<sub>2</sub>S catalysts prepared by an electrochemically driven cation exchange mechanism. To prepare such electrodes, pre-synthesised CoS<sub>x</sub> nanosheets based 3D structures were

taken as templates and a cation exchange reaction with Cu<sup>2+</sup> (where Co<sup>2+</sup> ions in CoS<sub>2</sub> were replaced with Cu<sup>1+/2+</sup> ions) was performed electrochemically in a 0.1 M LiClO<sub>4</sub>-dimethylformamide electrolyte solution containing 3 mM Cu(NO<sub>3</sub>)<sub>2</sub> by applying a potential of –0.47 V *vs.* normal hydrogen electrode for varied time periods. The amount of Co<sup>2+</sup> replaced with Cu<sup>2+</sup> ions was varied by controlling the charge passed during the electrochemical reaction. The formate production was found to be somewhat dependent on the percentage of Co<sup>2+</sup> ions exchanged by Cu<sup>2+</sup>. With a Cu<sub>2</sub>S sample obtained by passing 2.0 C of charge, 87.3% of formate was produced with a partial current density of 19 mA cm<sup>–2</sup> at –0.9 V *vs.* RHE in 0.1 M NaHCO<sub>3</sub> solution saturated with CO<sub>2</sub>. The authors reported that variation of the grain boundary obtained with the modulation of binary cations was the origin of the change in the product selectivity.

Ag is an excellent CO formation catalyst.<sup>104</sup> However, AgCu alloy can be designed to favour formate formation. Recent work on CuAg bimetallic nanoarchitectures demonstrated the importance of electronic and geometric modulation of the catalyst with respect to product selectivity.<sup>73</sup> The sponge-like Ag<sub>91</sub>Cu<sub>9</sub> and coralline Ag<sub>65</sub>Cu<sub>35</sub> nanoalloys prepared by anodising Ag<sub>52</sub>Cu<sub>39</sub>Sn<sub>9</sub> alloy foil induced a dramatic change in the selectivity of CO *versus* HCOOH. Changing the composition of the AgCu alloy, modifies the electronic arrangement of Ag and Cu and hence the binding strengths of intermediates as demonstrated by *in situ* Raman spectroscopic measurements shown in Fig. 7. Thus, on increasing the Cu content of the AgCu alloy, the selectivity shifted from favouring CO to forming formate with a faradaic efficiency of 96%.

Table 2 provides details of some state-of-the-art Cu alloys and other Cu based catalysts for selective formate production.

**4.1.2 CO.** Metals such as Zn,<sup>105–109</sup> Ag,<sup>110–114</sup> Au,<sup>115–119</sup> Pd,<sup>89,120–123</sup> which are highly selective for CO, have been alloyed with copper to enhance CO production in many studies. Post-transition metal such as In<sup>124–128</sup> and Sn<sup>129–133</sup> that are selective for formate generation also have been com-

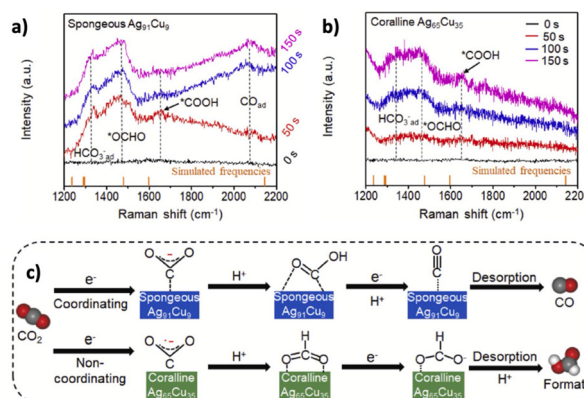


Fig. 7 (a and b) *In situ* Raman spectra obtained during electrolysis and (c) proposed reaction pathways on sponge-like Ag<sub>91</sub>Cu<sub>9</sub> and coralline Ag<sub>65</sub>Cu<sub>35</sub> alloy nanoarchitectures. Reprinted with permission.<sup>73</sup> Copyright 2020, Elsevier Ltd.

**Table 2** Examples of formate production with state-of-the-art Cu alloys and other Cu based catalysts

| Catalyst                                    | Electrolysis cell | Electrolyte                         | Potential (V vs RHE) <sup>a</sup> | FE (%) | $j_{\text{HCOO}^-}$ (mA cm <sup>-2</sup> ) | Ref. |
|---|-------------------|-------------------------------------|-----------------------------------|--------|--|------|
| Cu–Sn/rGO                                   | H-cell            | 0.5 M NaHCO <sub>3</sub>            | –1.0                              | 87.4   | 20.7                                       | 102  |
| Cu <sub>2</sub> S-2.0C                      | H-cell            | 0.1 M NaHCO <sub>3</sub>            | –0.9                              | 87.3   | 19.1                                       | 103  |
| Coralline Ag <sub>65</sub> Cu <sub>35</sub> | H-cell            | 0.1 M KHCO <sub>3</sub>             | –1.0                              | 91.8   | 16.8                                       | 73   |
| CuCd@Cu-20,45                               | H-cell            | 0.5 M NaHCO <sub>3</sub>            | –1.1                              | 70.1   | 26.8                                       | 99   |
| Porous Cu <sub>6,26</sub> Sn <sub>5</sub>   | H-cell            | 0.1 M KHCO <sub>3</sub>             | –1.1                              | 97.8   | ~30  | 136  |
| CuBi-100                                    | H-cell            | 0.5 M KHCO <sub>3</sub>             | –1.0                              | 94.7   | 13   | 137  |
| Cu/Au                                       | H-cell            | 0.5 M KHCO <sub>3</sub>             | –0.6                              | 81     | 10.4                                       | 138  |
| Sn–Cu                                       | H-cell            | 0.1 M KHCO <sub>3</sub>             | –0.95                             | 92     | ~10  | 139  |
| Cu@Sn nanocones                             | H-cell            | 0.1 M KHCO <sub>3</sub> + 0.3 M KCl | –1.1                              | 90.4   | 52   | 140  |
| CuSn alloy@Cu doped SnO                     | H-cell            | 0.5 M KHCO <sub>3</sub>             | –1.2                              | 95.4   | 30.3                                       | 141  |
| Cu <sub>11.5</sub> In <sub>88.5</sub> -OH   | H-cell            | 0.1 M KHCO <sub>3</sub>             | –1.1                              | 85     | ~10  | 142  |
| MOF derived CuBi                            | H-cell            | 0.5 M KHCO <sub>3</sub>             | –0.77                             | 100    | 67.9                                       | 143  |
| Cu <sub>2</sub> O/CuO/CuS                   | H-cell            | 0.1 M KHCO <sub>3</sub>             | –0.7                              | 84     | 20   | 144  |
| CuBi NPs                                    | H-cell            | 0.1 M KHCO <sub>3</sub>             | –0.99                             | 96     | 12.5                                       | 145  |
| CuS   | H-cell            | 0.1 M KHCO <sub>3</sub>             | –0.8                              | 80     | 18   | 146  |
| HCS/Cu-0.12                                 | H-cell            | 0.5 M KHCO <sub>3</sub>             | –0.81                             | 82.4   | 26   | 147  |
| S-doped OD-Cu                               | H-cell            | 0.1 M KHCO <sub>3</sub>             | –0.8                              | 73.6   | 13.9                                       | 148  |
| Cu <sub>6</sub> Sn <sub>5</sub> /Sn         | Flow cell         | 1 M KOH                             | –1.0                              | 86.7   | 103  | 149  |
| CuSn/Sn                                     | Flow cell         | 1 M KHCO <sub>3</sub>               | –0.7                              | 84.2   | ~26  | 150  |
| CuBi  | MEA               | 0.5 M KHCO <sub>3</sub>             | –1.07                             | 98.3   | 55.6                                       | 151  |

<sup>a</sup> Potential at which maximum FE was obtained.

combined with copper to tune the selectivity towards CO. This was achieved by alloying copper with metals where in most of the cases, at least one of the following situations exists: the alloy possesses (i) copper in an oxidized form, (ii) a lattice mismatch between the copper phase and the guest metal phase, (iii) a higher shared boundary between the copper and guest metal phases. Consequently, synergistic geometric and electronic effects emerge which influence product formation. Various factors influencing the CO selectivity over the copper-based bimetallic alloys are discussed below.

In early studies in the 1990s, Watanabe *et al.*<sup>55,134</sup> prepared CuZn alloys electrodes by electroplating onto gold electrodes and studied the eCO<sub>2</sub>RR efficiency in 0.05 M KHCO<sub>3</sub> electrolyte. They reported that higher concentrations of Zn in the CuZn alloy led to an increase in CO generation compared to the use of pure Cu. The only other eCO<sub>2</sub>RR product found was HCOO<sup>–</sup>. The Berlinguette group<sup>135</sup> studied eCO<sub>2</sub>RR using brass and bronze catalysts. They prepared 21 catalysts with varying Cu : Zn : Sn ratios by drop casting methanolic solutions of Cu, Zn, and/or Sn in the required proportions onto a titanium substrate followed by multiple exposures to near-infrared radiation and electroreduction to produce alloy films. Four-hour eCO<sub>2</sub>RR experiments with these film electrodes generated H<sub>2</sub>, CO and HCOOH as products. Cu–Zn–Sn alloys with Sn < 20% generated mainly syngas with the H<sub>2</sub> : CO ratio depending on the ratio between Cu and Zn. Hu *et al.*<sup>152</sup> prepared Cu–Zn catalysts by annealing a brass substrate at 500 °C in an Ar atmosphere prior to electroreduction of ZnO formed in the Zn metal annealing step, as shown in Fig. 8(a). On annealing, uniform 200 nm particles formed over the brass substrate. Zn and Cu have different melting points of 419.5 °C and 1085 °C, respectively. Accordingly, Zn melts at 500 °C and migrates all over the surface and is then converted to ZnO on exposure to air while Cu remains unchanged. The resultant catalyst used

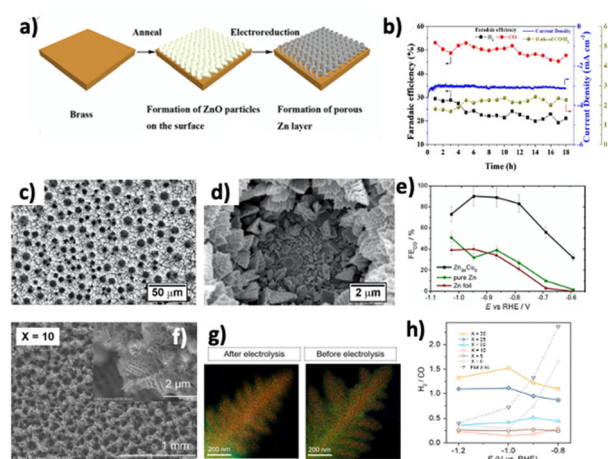


**Fig. 8** (a) Schematic illustration of the preparation of Zn–Cu catalysts from brass foil, (b) faradaic efficiencies, current density and CO/H<sub>2</sub> ratio obtained during eCO<sub>2</sub>RR as a function of time. Reprinted with permission.<sup>152</sup> Copyright 2018, Elsevier B.V. (c and d) SEM images of the Zn<sub>94</sub>Cu<sub>6</sub> catalyst, (e) CO faradaic efficiencies obtained with designated CuZn and Zn catalysts. Reprinted with permission.<sup>153</sup> Copyright 2018, the American Chemical Society. (f) SEM, (g) scanning transmission electron microscope – energy-dispersive X-ray spectroscopy (STEM-EDXS) mapping images of Zn<sub>90</sub>Cu<sub>10</sub> catalyst (h) ratio of H<sub>2</sub>/CO faradaic efficiencies obtained with designated Zn<sub>100–x</sub>Cu<sub>x</sub> catalysts. Reprinted with permission.<sup>154</sup> Copyright 2019, Wiley-VCH Verlag GmbH & Co. KGaA, Weinheim.

for eCO<sub>2</sub>RR over a range of applied potentials produced syngas with a 2 : 1 ratio of CO : H<sub>2</sub> (Fig. 8(b)) which is suitable for the Fischer–Tropsch process. The Broekmann group<sup>153</sup> synthesised Zn<sub>94</sub>Cu<sub>6</sub> alloy foams, as displayed in Fig. 8(c and d), by dynamic hydrogen bubble template assisted electrodeposition onto a Cu plate. eCO<sub>2</sub>RR with this catalyst produced 90% CO at –0.95 V vs. RHE in aqueous 0.5 M KHCO<sub>3</sub> electrolyte

(Fig. 8(e)). Lamaison *et al.*<sup>154</sup> also designed Cu–Zn alloy foam catalysts by electrodeposition of Cu onto Zn plates in their eCO<sub>2</sub>RR application. These foams were composed of a dendritic CuZn alloy structure (Fig. 8(f and g)). As shown in Fig. 8(h), bulk electrolysis experiments performed under eCO<sub>2</sub>RR conditions with 0.1 M CsHCO<sub>3</sub> as the electrolyte revealed an increase in the H<sub>2</sub> : CO ratio with increasing Cu content.

CuAu alloys, like CuZn ones, have been extensively studied for eCO<sub>2</sub>RR generation of CO. For example, enhancement of CO at Au<sub>x</sub>Cu<sub>100-x</sub> alloy catalysts has been reported by Christophe *et al.*<sup>155</sup> In particular, a significant increase in the production of CO was observed with use of an Au<sub>50</sub>Cu<sub>50</sub> catalyst. CO desorption at Au sites is promoted by the presence of adsorbed CO on Cu sites due to dipole repulsion between CO molecules at adjacent sites. Consequently, the presence of both Cu and Au in an optimal ratio enhances CO product formation. Bimetallic AuCu catalysts also induce an electronic effect which results in the shift in the d-band centre and hence changes the binding strength of the reaction intermediates. As a result of the shift in the d-band centre, the way the metals in the AuCu alloy interact with adsorbed intermediate also changes. The implication of this feature was examined by Kim *et al.*<sup>156</sup> who found that the evolution of CO increases with increasing Au content in the AuCu alloy. In the case of Au<sub>3</sub>Cu, they reported a mass activity (*i.e.* current density normalised to the amount of catalyst loaded) exceeding 200 A g<sup>-1</sup> at -0.73 V *versus* RHE, which represents a ten-fold increase in comparison with pure Cu. Surface valence band photoemission spectral analysis suggested that the improved selectivity towards CO with Au<sub>3</sub>Cu could also be due to the synergistic electronic and geometric effects associated with AuCu nanoparticle formation that occurred during the eCO<sub>2</sub>RR. The atomic arrangement of Au and Cu in AuCu bimetallic alloy nanoparticles (either ordered or disordered) also can have an impact. Among AuCu alloy nanoparticles, the nanoparticles with an ordered arrangement of Au and Cu (o-AuCu) exhibited a factor of two improvement in selectivity for CO (Fig. 9(a)).<sup>157</sup> STEM (Fig. 9(b)) and X-ray absorption spectroscopy (XAS) (Fig. 9(c)) analyses revealed that a thin layer of segregated Au atoms was formed on the surface of o-AuCu nanoparticles during electrolysis. DFT calculations suggested that the lattice strain of 6% associated with the Au layer due to the underlying AuCu lattice affected the catalytic activity of o-AuCu nanoparticles.

Intermetallic CuPd alloy catalysts provide another example of a Cu alloy that enhances CO generation during the eCO<sub>2</sub>RR process.<sup>159–161</sup> Excellent selectivity for CO with a faradaic efficiency of 86% and a partial current density of 6.9 mA cm<sup>-2</sup> was obtained on Pd<sub>85</sub>Cu<sub>15</sub> alloy nanoparticles (Fig. 10(a and b)).<sup>158</sup> On increasing the Cu content in the alloy, the efficiency decreased. X-ray absorption near edge structure (XANES) analysis shown in Fig. 10(c and d) for the PdCu alloy nanoparticles revealed that variation in Pd–Pd and Cu–Cu bond lengths alters the binding strengths of the CO<sub>2</sub> reduction intermediate (\*CO). Further, the formation of Pd and Cu oxides at higher Cu to Pd ratios leads to suppression of CO evolution during

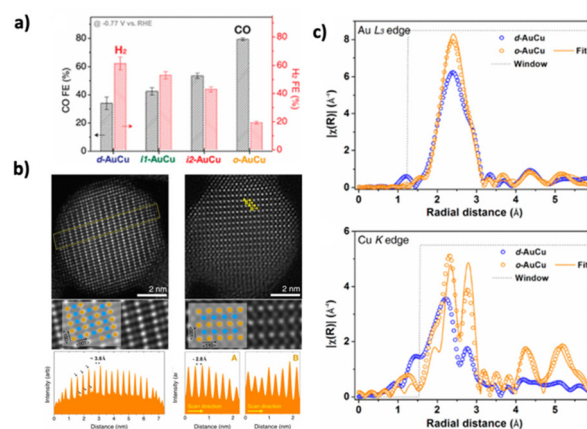


**Fig. 9** (a) Faradaic efficiencies for generation of H<sub>2</sub> and CO using AuCu alloy nanoparticles with designated atomic ordering, (b) high-angle annular dark-field imaging – scanning transmission electron microscope (HAADF – STEM) analysis of ordered AuCu nanoparticles, and (c) XAS analysis of ordered and disordered AuCu nanoparticles. Reprinted with permission.<sup>157</sup> Copyright 2017, the American Chemical Society.

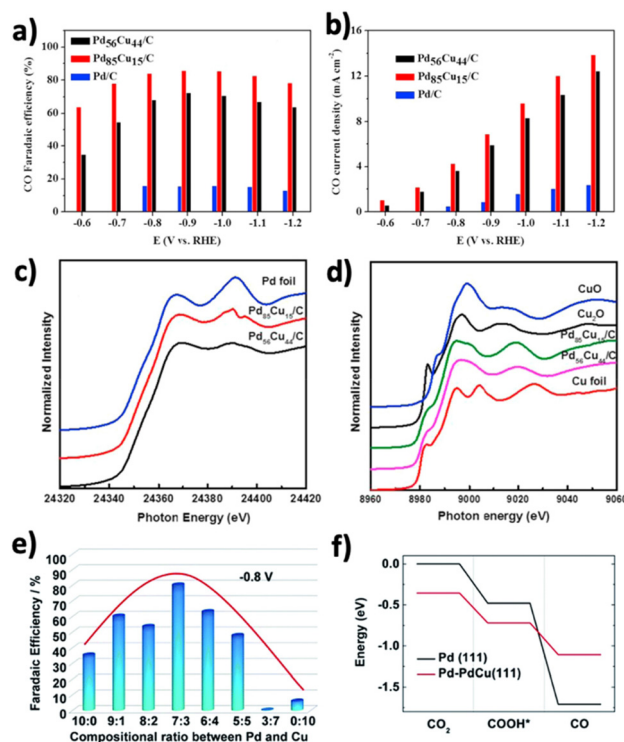


**Fig. 10** (a) CO faradaic efficiency Pd<sub>x</sub>Cu<sub>y</sub> nanoparticles, (b) CO partial current densities obtained using designated Pd<sub>x</sub>Cu<sub>y</sub> nanoparticles. (c) Pd K edge, and (d) Cu K edge XANES spectrum of a PdCu/C catalyst. Reprinted with permission.<sup>158</sup> Copyright 2016, Elsevier Ltd. (e) A comparison of CO selectivity at PdCu NPs with specified compositions, (f) free energy diagram for CO<sub>2</sub>, \*COOH and CO on a Pd terminated PdCu (111) surface. Reprinted with permission.<sup>159</sup> Copyright 2016, the Royal Society of Chemistry.

electrolysis. CuPd alloys with a 1.5 : 8.5 atomic ratio bind CO less strongly on the surface than with pure Pd, resulting in an enhancement of CO production.



The study by Li *et al.*<sup>159</sup> with mesoporous CuPd alloys also shows composition-dependent activity for CO<sub>2</sub> conversion (Fig. 10(e)). An alloy with a Cu to Pd ratio of 3 : 7 gives high CO yields, which diminishes with an increase in the Cu content. DFT calculations predict that Pd terminated Pd<sub>7</sub>Cu<sub>3</sub> alloy surfaces faceted with (111) planes will favour adsorption of a \*COOH intermediate and weaken adsorption ability of \*CO resulting in excellent CO selectivity (Fig. 10(f)). Due to the differences in electronegativity of Cu and Pd, the presence of Cu atoms adjacent to Pd in a Cu–Pd alloy increases the adsorption of \*COOH and CO on Pd surfaces, making Pd sites the active sites for the eCO<sub>2</sub>RR.

Oxide derived Cu–M (M = In/Sn) catalysts have been surveyed for their ability to convert CO<sub>2</sub> to CO. In and Sn in their metallic,<sup>162</sup> oxide<sup>163–165</sup> or chalcogenide<sup>166–168</sup> forms produce HCOO<sup>−</sup> from the eCO<sub>2</sub>RR. However, when oxides of these post-transition metals are combined with copper, scaling relationships can be altered due to synergistic effects associated with the lattice mismatch between Cu/CuO and MO<sub>2</sub> (M = In/Sn). The result is that product selectivity is shifted from formate to

CO with remarkably high faradaic efficiencies. For example, the study by Li *et al.*,<sup>169</sup> shows that the change in product distribution as a function of the thickness of the SnO<sub>2</sub> coated onto Cu nanoparticles (Fig. 11(b and c)). With a thin SnO<sub>2</sub> shell (0.8 nm), the product selectivity for CO had a FE of >90% at −0.6 V vs. RHE with little formate produced. In contrast, with a thick SnO<sub>2</sub> shell (1.8 nm), the eCO<sub>2</sub>RR behaviour is similar to that at Sn and formate is the major product. According to the results of DFT calculations, the synergistic effect emerged because of the compression strain and self-doping of Cu into the thinner SnO<sub>2</sub> shell layer during electrolysis which shifted selectivity from HCOO<sup>−</sup> to CO. A related study using Cu–In<sub>2</sub>O<sub>3</sub> core-shell nanoparticles (Fig. 11(d))<sup>170</sup> also showed that the thinnest shell provided a shift in selectivity to CO (Fig. 11(e and f)). With the thinner In<sub>2</sub>O<sub>3</sub> shell, the lattice mismatch between Cu and In<sub>2</sub>O<sub>3</sub> facilitates self-doping of Cu into the In<sub>2</sub>O<sub>3</sub> shell resulting in alteration of binding energies of \*COOH and \*OCHO intermediates, which leads to the generation of CO and HCOOH, respectively. Cu oxide surfaces decorated with Sn also enhance conversion of CO<sub>2</sub> to CO.

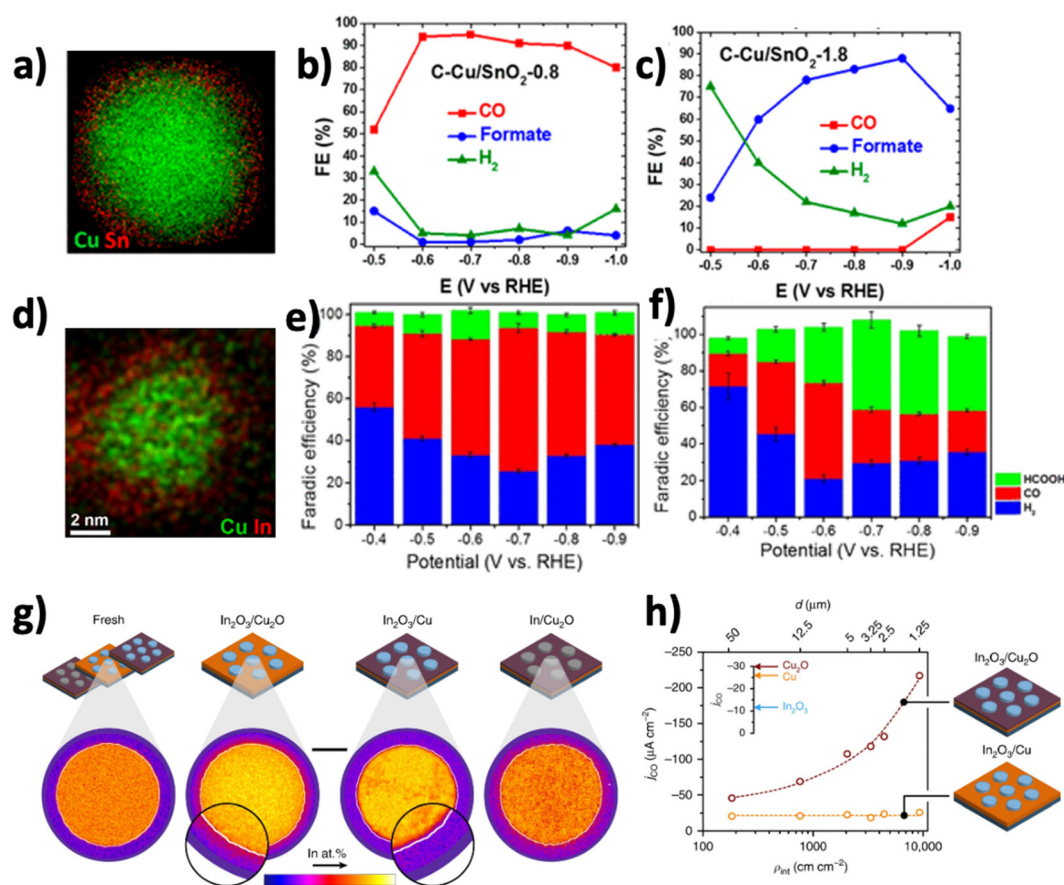


**Fig. 11** (a) Electron energy loss spectroscopy (EELS) elemental mapping of Cu/SnO<sub>2</sub> nanoparticles. (b) and (c) faradaic efficiencies of products obtained during eCO<sub>2</sub>RR with Cu/SnO<sub>2</sub> NPs having a shell thickness of (b) 0.8 nm and (c) 1.8 nm. Reprinted with permission.<sup>169</sup> Copyright 2017, the American Chemical Society. (d) EDS elemental mapping of C–Cu/In<sub>2</sub>O<sub>3</sub> nanoparticles. (e) and (f) faradaic efficiencies of products obtained during eCO<sub>2</sub>RR with Cu/In<sub>2</sub>O<sub>3</sub> nanoparticles having a shell thickness of (e) 0.4 nm and (f) 1.5 nm. Reprinted with permission.<sup>170</sup> Copyright 2018, the American Chemical Society. (g) elemental mapping showing the formation of indium islands when undertaking eCO<sub>2</sub>RR with CuIn electrodes, (h) CO partial current density obtained during eCO<sub>2</sub>RR at −0.6 V with In<sub>2</sub>O<sub>3</sub>/Cu<sub>2</sub>O and In<sub>2</sub>O<sub>3</sub>/Cu electrodes as a function of island diameter and interfacial density. Reprinted with permission.<sup>171</sup> Copyright 2018, Nature Publishing Group.

Zhao *et al.*<sup>172</sup> decorated electrochemically generated CuO nanowires with Sn. An optimal loading of Sn produced 90% of CO at  $-0.8$  V vs. RHE in 0.1 M KHCO<sub>3</sub> electrolyte. Sarfraz *et al.*<sup>173</sup> electrochemically deposited Sn on a Cu sheet. With a Sn loading of 3.9 mol cm<sup>-2</sup>, 90% of CO was obtained at  $-0.6$  V vs. RHE in 0.1 M KHCO<sub>3</sub>. However, with higher Sn loadings, selectivity reverted to HCOO<sup>-</sup>. Zeng *et al.*<sup>174</sup> used Cu–Sn foam based dendritic structures, where the Cu dendrites were decorated with small amounts of SnO<sub>x</sub> to form a Cu/CuO<sub>x</sub>–SnO<sub>x</sub> core/shell structure. This allowed 93–94% CO to be formed between  $-0.75$  V and  $-0.9$  V vs. RHE in 0.1 M KHCO<sub>3</sub>.

Studies by the Takanabe group<sup>175,176</sup> employing In coated on oxide derived (OD)-Cu<sup>175</sup> and CuInO<sub>2</sub> derived Cu–In alloy<sup>176</sup> catalysts again revealed a drastic increase in CO selectivity. DFT calculations suggest that the replacement of a Cu atom with an In atom would suppress \*H adsorption with \*CO adsorption energy unchanged, resulting an increase in the FE of CO while decreasing HER. A study by Larrazábal *et al.*<sup>177</sup> proposed that an *in situ* generated metastable In(OH)<sub>3</sub> phase in the oxide plays an important role in the use of Cu–In catalysts. The core–shell structured Cu–In catalysts, with In(OH)<sub>3</sub> as the shell evolved upon repeated voltammetric cycles of potential on the initial Cu–In in a 0.1 M KHCO<sub>3</sub> solution, exhibited a significant increase in the CO selectivity. The same group also reported the dependence of CO selectivity on the nature of the Cu–In interfaces.<sup>171</sup> In their study, the authors microfabricated In<sub>2</sub>O<sub>3</sub> dots on Cu and Cu<sub>2</sub>O surfaces. In<sub>2</sub>O<sub>3</sub> dots on Cu left the selectivity unaltered, whereas those on Cu<sub>2</sub>O led to a drastic improvement in selectivity for CO. When the interfacial density is low, both catalysts showed similar activity. However, when the density of metal–oxide interface was increased, the catalytic activity towards CO was enhanced with In<sub>2</sub>O<sub>3</sub>/Cu<sub>2</sub>O, as shown in Fig. 11(h). The irregular layer of Cu formed by reduction of Cu<sub>2</sub>O enhances the diffusion of In (Fig. 11(g)) giving rise to a synergistic effect at Cu–In interfaces. This study reveals that both the interfaces and Cu<sub>2</sub>O are essential for achieving synergistic effects that tune the selectivity pathway.

State of the art Cu alloys and other Cu based catalysts that favoured CO production are tabulated in Table 3.

## 4.2 Highly reduced C<sub>1</sub> products

**4.2.1 Methane.** The formation of methane on Cu based bimetallic catalysts with the eCO<sub>2</sub>RR was reported in early literature using Cu modified Pd and PdH catalysts.<sup>100,101</sup> The amount of hydrogen absorbed in PdH has a significant effect on the selectivity for methane. For instance, the methane production was enhanced initially at Cu–PdH catalysts with lower coverages of adsorbed H on Pd. However, there was no further increase in CH<sub>4</sub> at higher concentrations of adsorbed H.

Electrochemical conversion of CO<sub>2</sub> to methane has been explored on Cu–Zn catalysts. Cuenya and co-workers<sup>184</sup> studied the eCO<sub>2</sub>RR product selectivity dependence on the composition and structure of CuZn nanoparticles derived from adoption of the inverse micelle encapsulation method. Their bulk electrolysis eCO<sub>2</sub>RR experiments with Cu<sub>100-x</sub>Zn<sub>x</sub> revealed the presence of Zn from 10% to 50% increased CH<sub>4</sub> formation while higher 50% Zn levels suppressed CH<sub>4</sub> formation and increased that of CO (Fig. 12(a)). The XANES studies suggested that the Cu–ZnO interface is needed to generate CH<sub>4</sub> or other hydrocarbons while CuZn (brass) alloy favours formation of CO/H<sub>2</sub> mixtures. Due to the faster reduction rate with CuO than with ZnO, in samples with a lower Zn content (Cu<sub>100-x</sub>Zn<sub>x</sub>,  $x < 50$ ), the Cu–ZnO interface prevailed in the initial period of time during eCO<sub>2</sub>RR, when the hydrogenation of CO species was favoured at Cu sites. When both oxides were fully reduced, brass nanoparticles were generated so that Cu loses its ability to stabilise \*CH<sub>y</sub> ( $y = 1-3$ ) intermediates due to ligand effects and hence CO and H<sub>2</sub> were released as the electrolysis products.

Ceria (CeO<sub>2</sub>) is another material that facilitates CH<sub>4</sub> production in the presence of Cu sites during eCO<sub>2</sub>RR.<sup>185</sup> Doping CeO<sub>2</sub> nanorods with Cu establishes a strong interaction between atomically dispersed Cu sites and CeO<sub>2</sub>. Accordingly, multiple oxygen vacancies are induced around Ce under eCO<sub>2</sub>RR conditions, which provides an effective site for electro-

**Table 3** Examples of the state-of-the-art Cu alloys and other Cu based catalysts that favour CO production

| Catalyst                                   | Electrolysis cell     | Electrolyte             | Potential (V vs. RHE) <sup>a</sup> | FE (%) | $j_{CO}$ (mA cm <sup>-2</sup> ) | Ref. |
|--|-----------------------|-------------------------|------------------------------------|--------|---------------------------------|------|
| Zn <sub>94</sub> Cu <sub>6</sub> nanofoam  | H-cell                | 0.5 M KHCO <sub>3</sub> | $-0.9$                             | 90     | ~4.5                            | 153  |
| o-AuCu NPs                                 | H-cell                | 0.1 M KHCO <sub>3</sub> | $-0.8$                             | ~80    | 1.4                             | 157  |
| Mesoporous Pd <sub>7</sub> Cu <sub>3</sub> | H-cell                | 0.1 M KHCO <sub>3</sub> | $-0.8$                             | 80     | ~1.5                            | 159  |
| Pd <sub>85</sub> Cu <sub>15</sub> /C       | H-cell                | 0.1 M KHCO <sub>3</sub> | $-0.9$                             | 86     | 6.9                             | 158  |
| C–Cu/SnO <sub>2</sub> -0.8                 | H-cell                | 0.5 M KHCO <sub>3</sub> | $-0.7$                             | 93     | ~13                             | 169  |
| Cu–Sn10 nanowires                          | H-cell                | 0.1 M KHCO <sub>3</sub> | $-0.8$                             | 90     | 4.5                             | 172  |
| Cu–Sn                                      | H-cell                | 0.1 M KHCO <sub>3</sub> | $-0.6$                             | 90     | 1.0                             | 173  |
| Cu–Sn foam                                 | H-cell                | 0.1 M KHCO <sub>3</sub> | $-0.8$                             | 94     | 3                               | 174  |
| PTFE-Cu                                    | H-cell                | 0.1 M KHCO <sub>3</sub> | $-0.4$                             | 71     | 1.5                             | 178  |
| Cu NPs-700                                 | H-cell                | 0.1 M KHCO <sub>3</sub> | $-0.6$                             | 75.6   | 3.8                             | 179  |
| Cu–N <sub>2</sub> /GN                      | H-cell                | 0.1 M KHCO <sub>3</sub> | $-0.5$                             | 81     | ~2                              | 180  |
| Cu/CNT                                     | PEM Cell <sup>b</sup> | 0.1 M KHCO <sub>3</sub> | $-3.5^c$                           | 75.7   | 12.2                            | 181  |
| CuPd nanosheets                            | Flow cell             | 1 M KOH                 | $-0.6$                             | 71     | 58                              | 161  |
| 2.7 nm PdCu NPs                            | Flow cell             | 1 M KOH                 | $-1.0$                             | 82     | 80                              | 182  |
| Sb–Cu <sub>2</sub> O                       | Flow cell             | 0.1 M KOH               | $-0.8$                             | 96     | 60                              | 183  |

<sup>a</sup> Potential at which maximum FE was obtained. <sup>b</sup> Polymer electrolyte membrane electrolysis cell. <sup>c</sup> Cell voltage.

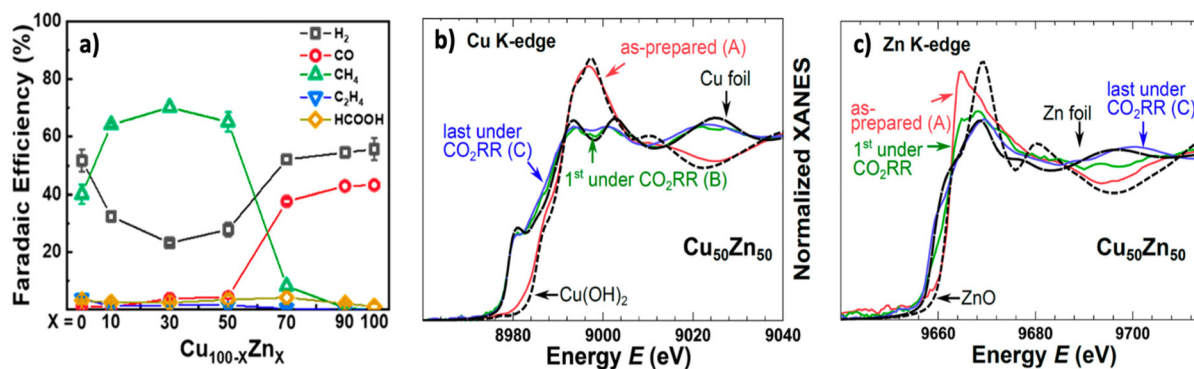


**Fig. 12** (a) A comparison of faradaic efficiencies for the products obtained by eCO<sub>2</sub>RR with Cu<sub>100-x</sub>Zn<sub>x</sub> catalysts, (b) Cu K-edge and (c) Zn K-edge XANES spectra of Cu<sub>50</sub>Zn<sub>50</sub> nanoparticles: spectrum A – as-prepared sample, spectrum B – immediately after the onset of eCO<sub>2</sub>RR and spectrum C – after 7 h of electrolysis. Reprinted with permission.<sup>184</sup> Copyright 2019, the American Chemical Society. Source: <https://pubs.acs.org/doi/10.1021/jacs.9b10709>. Further permissions related to the material excerpted should be directed to the ACS.

catalytic reduction of CO<sub>2</sub> to CH<sub>4</sub>. CeO<sub>2</sub> nanorods doped with 4% Cu produce ~58% of CH<sub>4</sub> at -1.8 V vs. RHE with a current density of 56 mA cm<sup>-2</sup> in 0.1 M KHCO<sub>3</sub>, as shown in Fig. 13(b). The Buonsanti group<sup>186</sup> has explained the importance of the interaction between CeO<sub>2</sub> and Cu in facilitating CH<sub>4</sub> formation by examining outcomes of the eCO<sub>2</sub>RR with Cu/CeO<sub>2</sub> heterodimer (HD) nanoparticles as well as physical mixtures of Cu and CeO<sub>2</sub> nanoparticles. In addition to the presence of CeO<sub>2</sub> interactions with Cu nanoparticles described above, the size of the Cu nanoparticles was shown to play a significant role in the improvement in CH<sub>4</sub> selectivity. The 36 nm sized Cu/CeO<sub>2</sub> HD nanoparticles enhanced eCO<sub>2</sub>RR per-

formance over HER and the selectivity achieved for CH<sub>4</sub> reached 54% at -1.2 V vs. RHE in 0.1 M KHCO<sub>3</sub>. In contrast, the Cu and CeO<sub>2</sub> physical mixture resulted in only <10% of methane. XAS data (Fig. 13(d)) confirmed that during eCO<sub>2</sub>RR, Ce<sup>4+</sup> in Cu/CeO<sub>2</sub> HD is reduced to Ce<sup>3+</sup>. On the basis of DFT calculations, the eCO<sub>2</sub>RR intermediates (\*COOH, \*CHO, H<sub>2</sub>CO\*, H<sub>3</sub>CO\*) were postulated to be adsorbed onto both Cu and Ce sites with an O-vacancy in order to form CH<sub>4</sub>. Thus, oxygen vacancies played a crucial role in enhancing methane selectivity.

Chang *et al.*<sup>187</sup> have studied the impact of structural reconstruction of Cu<sub>100-x</sub>Ag<sub>x</sub> catalysts on product selectivity using the techniques of *in situ* grazing-angle X-ray scattering/diffraction, X-ray absorption spectroscopy, and Raman spectroscopy. The authors showed that Cu<sub>68</sub>Ag<sub>32</sub> nanowires underwent dynamic oxidation–reduction cycles on the nanowire surface resulting in an inter diffusion of Ag and Cu atoms prior to stabilization of the metallic states of Cu and Ag. The high methane FE of 60% is three times to that achieved with pristine Cu nanowire.

**4.2.2 Methanol.** Early studies by Watanabe *et al.*<sup>55,193</sup> on the electrochemical generation of CH<sub>3</sub>OH by reduction of CO<sub>2</sub> used Cu based alloys, particularly CuNi ones. Enhancement of methanol selectivity was reported by Jia *et al.*<sup>194</sup> using a AuCu alloy catalyst deposited electrochemically onto a nanoporous Cu film (NCF). The FE for methanol production was dependent on the alloy composition. With a Cu<sub>63.9</sub>Au<sub>36.1</sub>/NCF catalyst, a FE of 15.9% was achieved which was 19 times higher than with pristine Cu.

Albo *et al.*<sup>195</sup> studied the use of Cu<sub>2</sub>O/ZnO catalysts for eCO<sub>2</sub>RR in a flow cell using electrodes prepared by airbrushing commercially available Cu<sub>2</sub>O and ZnO nanoparticles over carbon paper. They found that the ratio of Cu<sub>2</sub>O/ZnO has a significant effect on methanol generation during eCO<sub>2</sub>RR. Cu<sub>2</sub>O/ZnO with 2 : 1 ratio generated a high selectivity for methanol with a FE of 25.2% at -1.3 V vs. Ag/AgCl (sat. KCl) in 0.5 M KHCO<sub>3</sub>. Recently, Bagchi *et al.*<sup>192</sup> reported excellent selectivity towards methanol could be achieved with an intermetallic

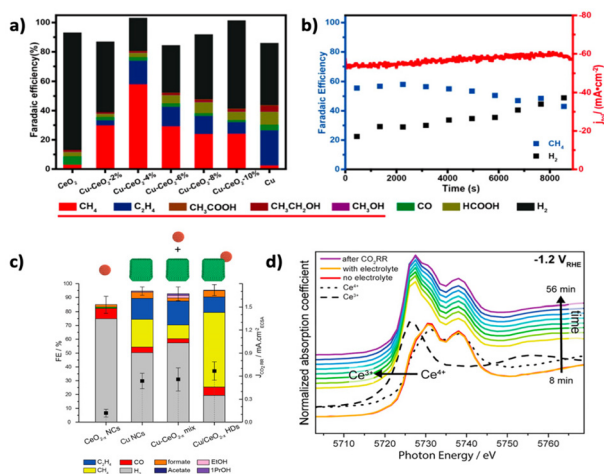


**Fig. 13** (a) Comparison of product selectivity obtained with Cu doped CeO<sub>2</sub> catalysts, (b) long term stability of a Cu–CeO<sub>2</sub>-4% (4% of Cu doped in CeO<sub>2</sub>) catalyst at -1.2 V vs. RHE. Reprinted with permission.<sup>185</sup> Copyright 2018, the American Chemical Society. (c) Product selectivity comparison and CO<sub>2</sub>RR partial current densities obtained with Cu/CeO<sub>2-x</sub> HDs, Cu–CeO<sub>2-x</sub> mixture, Cu nanocrystals (NCs), and CeO<sub>2-x</sub> NCs, (d) Ce L<sub>III</sub>-edge XANES spectra collected every eight minutes when using Cu/CeO<sub>2-x</sub> HDs under eCO<sub>2</sub>RR conditions at -1.2 V vs. RHE in 0.1 M KHCO<sub>3</sub>. Reprinted with permission.<sup>186</sup> Copyright 2019, the American Chemical Society.

CuGa<sub>2</sub> electrocatalyst. An exceptional FE of 77.6% for methanol was achieved at  $-0.3$  V vs. RHE. X-ray photoelectron spectroscopy (XPS) and *in situ* X-ray absorption fine structure (XAFS) analysis revealed the importance of surface and subsurface oxides of Ga at low potentials in enhancing methanol selectivity. However, when more negative potentials were applied, lattice expansion occurs, indicating reduction of Ga<sub>2</sub>O<sub>3</sub>, which resulted in the diminution of methanol selectivity.

Table 4 summarises state-of-the-art Cu alloys and other Cu based catalysts, which are selective for methane and methanol in H type and flow cells.

### 4.3 C<sub>2</sub>/C<sub>2+</sub> products

C–C coupling is required to produce C<sub>2</sub>/C<sub>2+</sub> products. Electrochemically reducing CO<sub>2</sub> to C<sub>2</sub> products with significant selectivity is a great challenge. Typically, copper is combined with transition metals that generate CO as their primary product during eCO<sub>2</sub>RR to improve the selectivity for C<sub>2</sub> products. With Cu–M (M = guest metal) bimetallic alloy catalysts, the formation of C<sub>2</sub> hydrocarbons is impacted by two main effects: the spillover of CO at the boundaries and electronic effects. The geometric arrangement of the Cu and guest metal

**Table 4** Examples of the state-of-the-art Cu alloys and other Cu catalysts that favour methane or methanol production

| Catalyst                                    | Product            | Electrolysis cell | Electrolyte                                 | Potential (V vs. RHE) <sup>a</sup> | FE (%) | <i>J</i> <sub>product</sub> (mA cm <sup>-2</sup> ) | Ref. |
|---|--------------------|-------------------|---|------------------------------------|--------|--|------|
| Cu–ZnO NPs                                  | CH <sub>4</sub>    | H-cell            | 0.1 M KHCO <sub>3</sub>                     | -1.35                              | 70     | ~40  | 184  |
| 4% Cu doped CeO <sub>2</sub>                | CH <sub>4</sub>    | H-cell            | 0.1 M KHCO <sub>3</sub>                     | -1.8                               | 58     | 33.6   | 185  |
| Cu <sub>68</sub> Ag <sub>32</sub> nanowires | CH <sub>4</sub>    | H-cell            | 0.5 M KHCO <sub>3</sub>                     | -1.2                               | 60     | ~27  | 187  |
| Cu foil                                     | CH <sub>4</sub>    | H-cell            | 0.5 M NaHCO <sub>3</sub> + methyl carbamate | -2.1                               | 85     | 31   | 188  |
| Single atom Cu/GYD                          | CH <sub>4</sub>    | H-cell            | 0.1 M KHCO <sub>3</sub>                     | -1.3                               | 66     | 20   | 189  |
| Single atom Cu/TCNFs                        | CH <sub>3</sub> OH | H-cell            | 0.1 M KHCO <sub>3</sub>                     | -0.9                               | 44     | 41   | 190  |
| Cu (111) nanospheres                        | CH <sub>4</sub>    | Flow cell         | 1 M KOH                                     | -0.91                              | 53     | 53   | 191  |
| CuGa <sub>2</sub>                           | CH <sub>3</sub> OH | Flow cell         | 1 M KOH                                     | -0.3                               | 78     | ~16  | 192  |

<sup>a</sup> Potential at which maximum FE was obtained.

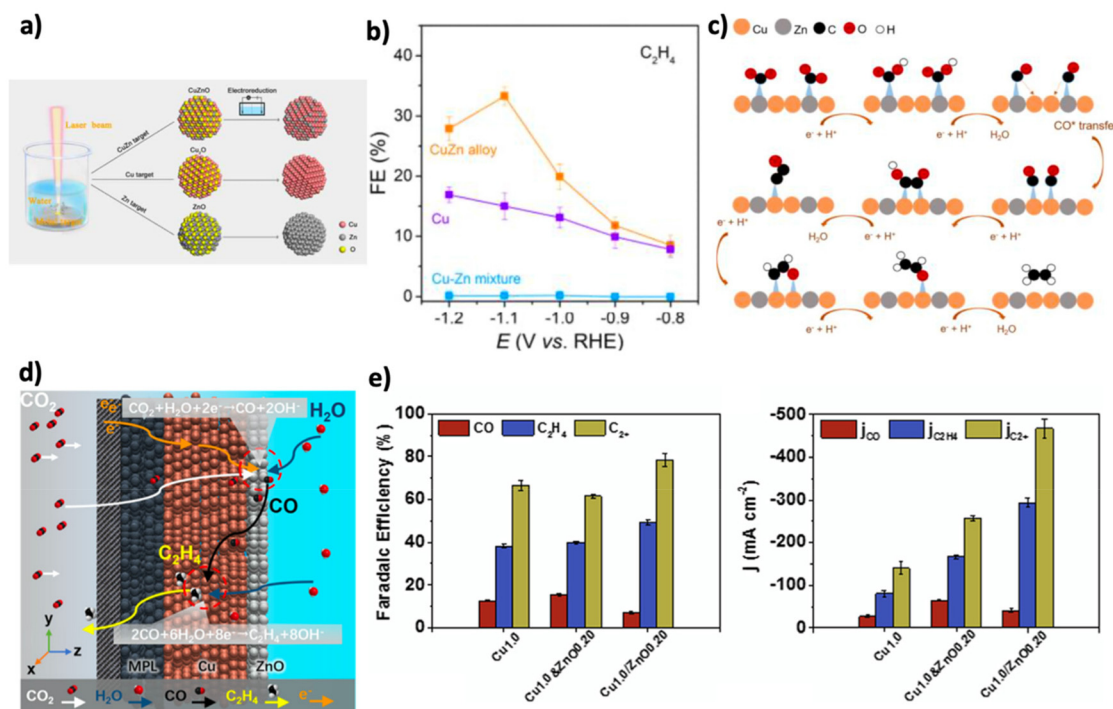


**Fig. 14** (a) Schematic representation of the preparation of CuZn alloy nanoparticles, (b) faradaic efficiency of C<sub>2</sub>H<sub>4</sub> obtained by eCO<sub>2</sub>RR using CuZn alloy, Cu–Zn mixtures and Cu catalysts, (c) mechanism proposed for C<sub>2</sub>H<sub>4</sub> formation with CuZn catalysts. Reprinted with permission.<sup>201</sup> Copyright 2018, the American Chemical Society; (d) schematic representation of use of a Cu–ZnO tandem catalyst to generate CO<sub>2</sub> → C<sub>2+</sub>, (e) faradaic efficiency and current density obtained with Cu, Cu and ZnO mixtures and Cu–ZnO tandem catalysts. Reprinted with permission.<sup>203</sup> Copyright 2020, Elsevier Inc.

in the catalyst leads to the emergence of phase boundaries which promote C–C coupling by increasing CO coverage and stabilising reaction intermediates. The identity and availability of the guest metal near Cu affects the concentration of CO at copper. The oxidation state of Cu in the catalyst also is significant in providing a selective pathway for ethylene or ethanol production during electrolysis. In particular, stabilisation of the Cu(I) state of the catalyst during eCO<sub>2</sub>RR has been suggested to be crucial for the generation of highly reduced carbons,<sup>36,196–199</sup> but not without debate.<sup>200</sup>

**4.3.1 Ethylene.** CuZn alloy nanoparticles, prepared by Feng *et al.*,<sup>201</sup> have been reported to produce ethylene with considerable selectivity, as depicted in Fig. 14(a and b). In their study, the authors initially prepared CuZn nanoparticles having different Cu : Zn ratios by the pulsed laser ablation method and electrochemically reduced them to CuZn before performing bulk electrolysis experiments. They found that CuZn nanoparticles with a 4 : 1 Cu : Zn ratio generated 33.3% ethylene at  $-1.15$  V vs. RHE in 0.1 M KHCO<sub>3</sub>. The reason for enhanced ethylene formation is the generation of abundant \*CO associated with the presence of Zn and also the homogeneous distribution of Cu and Zn in CuZn nanoparticles that aids the transfer of \*CO from Zn to Cu sites followed by CO–CO coupling over the Cu sites and then finally the release of C<sub>2</sub>H<sub>4</sub> (see Fig. 14(c)).

Garcia *et al.*<sup>202</sup> have synthesized CuO/ZnO particles by a water/oil microemulsion method. Bulk electrolysis experiments using this catalyst in 0.1 M KHCO<sub>3</sub> using a flow cell, produced ethylene with a faradaic efficiency of 91.1% at highly negative potentials ( $-2.5$  V vs. Ag/AgCl). Recently, Zhang *et al.*<sup>203</sup> prepared a Cu/ZnO tandem catalyst by airbrushing commercial Cu and ZnO nanoparticles over carbon paper and performed bulk electrolysis with a flow cell in 1 M KOH solution (Fig. 14(d)). With this Cu/ZnO tandem catalyst, the combination of ZnO acting as a CO generator and Cu as a C<sub>2</sub> intermediate stabilizer enhances C<sub>2</sub> and C<sub>2+</sub> product formation. With an optimal loading of Cu and ZnO, Cu/ZnO tandem catalyst produces 48% ethylene at  $-0.7$  V vs. RHE in 1 M KOH (Fig. 14(e)).

Use of uniformly distributed CuAg alloy nanowires prepared by electroplating in 3,5-diamino-1,2,4-triazole baths, significantly enhances C<sub>2</sub> product generation (ethylene in particular) during eCO<sub>2</sub>RR in a flow reactor.<sup>204</sup> The faradaic efficiency of  $\sim 60\%$  for ethylene at  $-0.7$  V vs. RHE and a total current density of 300 mA cm<sup>-2</sup> achieved with CuAg alloy nanowires containing 6% Ag, demonstrates superior CO<sub>2</sub> reduction activity as shown in Fig. 15(a). Examination of *in situ* Raman spectra shown in Fig. 15(b and c) led to the conclusion that high stability of Cu<sub>2</sub>O layers under electrolysis conditions and the optimal availability of CO were the factors that resulted in high C<sub>2</sub>H<sub>4</sub> selectivity. The

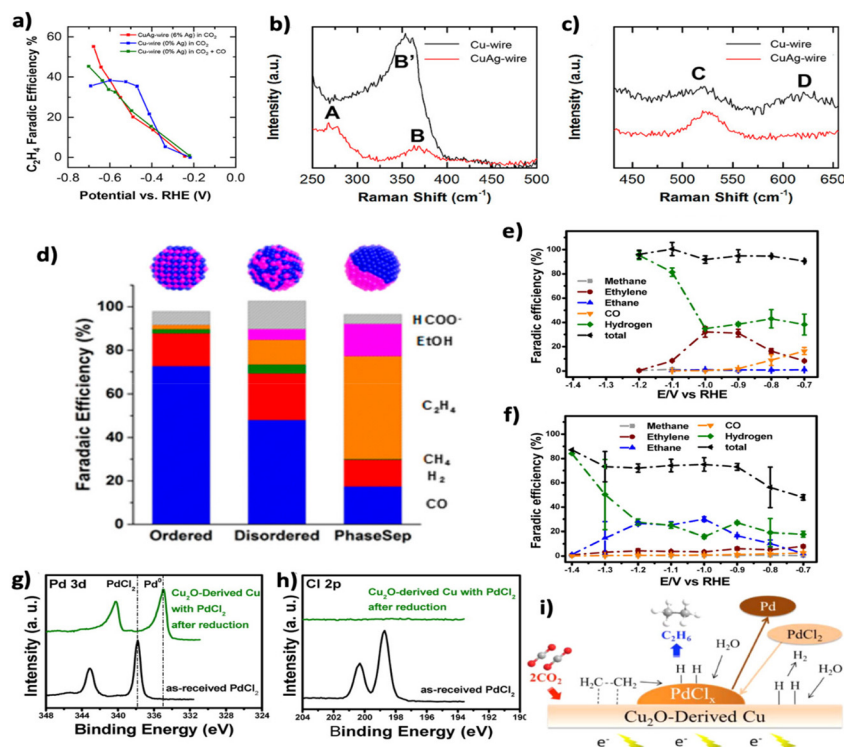


**Fig. 15** (a) Faradaic efficiencies for ethylene formation obtained during electrolysis at AgCu and Cu catalysts under different experimental conditions, (b and c) *in situ* Raman spectra showing (b) the Cu–CO stretch, and (c) the Cu–O stretch regions obtained from the eCO<sub>2</sub>RR using electrolysis AgCu and Cu catalysts at  $-0.7$  V in 0.1 M KOH solution. Reprinted with permission.<sup>204</sup> Copyright 2018, American Chemical Society. (d) Faradaic efficiencies of products obtained with three CuPd catalysts. Reprinted with permission.<sup>64</sup> Copyright 2017, the American Chemical Society. (e and f) eCO<sub>2</sub>RR product distribution obtained using Cu catalysts (e) with and (f) without PdCl<sub>2</sub> in the electrolyte, (g and h) XPS of (g) Pd 3d and (h) Cu 2p regions of PdCl<sub>2</sub> and a Cu catalyst with PdCl<sub>2</sub> after reduction, (i) schematic illustration of ethane formation from surface adsorbed ethylene and hydrogen using a Cu catalyst in the presence of PdCl<sub>2</sub>. Reprinted with permission.<sup>205</sup> Copyright 2015, the American Chemical Society.

importance of the geometric arrangement in tuning the product selectivity at copper-based bimetallic catalysts is emphasized by eCO<sub>2</sub>RR studies using alloys with different alloying configurations.<sup>64</sup> CuPd alloys with ordered, disordered, and phase-separated geometric structures have been examined for CO<sub>2</sub> reduction in 1 M KOH solution using a flow reactor. The phase-separated sample exhibited superior activity for C<sub>2</sub> product selectivity. A total FE for C<sub>2</sub> products of 63% was achieved at  $-0.8$  V vs. RHE, in which the contribution from ethylene was  $\sim 50\%$ , as shown in Fig. 15(d). On the other hand, the selectivity for ethylene at disordered alloy sample is  $\sim 4$  times lower than the phase separated sample. In contrast, the ordered CuPd alloy produced only C<sub>1</sub> products, mainly CO.

The significant role of PdCl<sub>2</sub> electrolyte in modifying the product selectivity achieved with Cu<sub>2</sub>O derived Cu catalysts was identified by Yeo and co-workers.<sup>205</sup> With a pure Cu<sub>2</sub>O derived Cu electrode, a 32% yield of ethylene was achieved  $-1.0$  V vs. RHE in an aqueous bicarbonate solution. With addition of PdCl<sub>2</sub> into the electrolyte, a complete shift in the major product was observed with selectivity changing from C<sub>2</sub>H<sub>4</sub> to C<sub>2</sub>H<sub>6</sub>. Now the highest faradaic efficiency was 30% for C<sub>2</sub>H<sub>6</sub> at the same potential (Fig. 15(e and f)). Analysis of XPS data after electrolysis (Fig. 15(g and h)) revealed that PdCl<sub>2</sub> provides the source of a sacrificial dopant by forming Pd<sup>0</sup> on Cu<sub>2</sub>O during the electrolysis reaction. According to the authors, the Pd<sup>0</sup> sites adsorb hydrogen effectively and provide a hydrogen source that facilitates reduction of C<sub>2</sub>H<sub>4</sub> to C<sub>2</sub>H<sub>6</sub>, as shown in Fig. 15(i).

Tables 5 and 6 summarises the state-of-the-art Cu alloys and Cu based catalysts, which are selective for ethylene in H-type and flow cells, respectively.

**4.3.2 Ethanol.** The Yeo group<sup>243</sup> introduced oxide derived Cu<sub>x</sub>Zn catalysts for improving the selectivity for ethanol. In their study, Cu<sub>x</sub>Zn catalysts were prepared by electrodeposition of Cu<sub>2</sub>O and ZnO layers onto a polished Cu disk from a solution containing CuSO<sub>4</sub> and ZnCl<sub>2</sub> with Cu : Zn ratios of 10, 4, 2 at a current density of  $-0.92$  mA cm<sup>-2</sup> for 600 s. Detailed characterization with selected area electron diffraction (SAED) and X-ray diffraction (XRD) techniques showed that the electrodeposited Cu<sub>x</sub>Zn consisted of phase segregated Cu and Zn crystallites rather than a CuZn alloy. eCO<sub>2</sub>RR experiments with phase segregated Cu<sub>x</sub>Zn catalysts revealed that Cu<sub>4</sub>Zn produced 29% ethanol at  $-1.05$  V vs. RHE in 0.1 M KHCO<sub>3</sub> with a partial current density of 8.2 mA cm<sup>-2</sup>. The ethanol/ethylene ratio was found to be positively correlated with the Zn content with the tested samples. On increasing the Zn content from 0% to 30% in Cu<sub>x</sub>Zn, the ethanol/ethylene ratio increased from 0.48 to 6. As shown in Fig. 16(a), it was proposed that CO generated at the Zn site spilt over to the Cu site and inserted into the \*CH<sub>2</sub> intermediate on the Cu surface, leading to the enhancement of ethanol generation.

The Grätzel group<sup>244</sup> reported that a CuO/ZnO core/shell structure derived CuZn bimetallic alloy catalyst for eCO<sub>2</sub>RR achieved 41% and 48% of C<sub>2+</sub> product selectivity in H-cell and flow cell configurations respectively, with ethanol being the primary C<sub>2</sub> product. To achieve this outcome, CuO nanowires

**Table 5** Examples of state-of-the art Cu alloys and other Cu based catalysts selective for ethylene generation in an H-cell by eCO<sub>2</sub>RR

| Catalyst                                      | Electrolysis cell                | Electrolyte                          | Potential (V vs. RHE) <sup>a</sup> | FE (%)    | $j_{C_2H_4}$ (mA cm <sup>-2</sup> ) | Ref. |
|---|----------------------------------|--------------------------------------|------------------------------------|-----------|-------------------------------------|------|
| OD-Cu + PdCl <sub>2</sub>                     | H-cell                           | 0.1 M KHCO <sub>3</sub>              | $-1.0$                             | 32        | $\sim 10$                           | 205  |
| ZrO <sub>2</sub> /Cu-Cu <sub>2</sub> O        | H-cell                           | 0.1 M KCl                            | $-1.3$                             | 62.5      | 15                                  | 206  |
| 4H crystal phased Au/Cu nanoribbon            | H-cell                           | 0.1 M KHCO <sub>3</sub>              | $-1.1$                             | 44.9      | 14.4                                | 207  |
| Ag/Nafion-Cu <sub>2</sub> O                   | Single compartment cell          | 0.1 M NaHCO <sub>3</sub>             | $-1.9$                             | 80        | 16                                  | 208  |
| Ag-Cu nanodimers                              | Custom made two compartment cell | 0.1 M KHCO <sub>3</sub>              | $-1.1$                             | $\sim 40$ | 10                                  | 209  |
| Anodized Cu                                   | PEEK <sup>b</sup>                | 0.1 M KHCO <sub>3</sub>              | $-1.08$                            | 38.1      | 7.3                                 | 210  |
| Plasma activated Cu                           | Custom made two compartment cell | 0.1 M KHCO <sub>3</sub>              | $-0.9$                             | 60        | $>8$                                | 211  |
| Cu <sub>2</sub> O derived Cu                  | Teflon cell <sup>b</sup>         | 0.1 M KHCO <sub>3</sub>              | $-1.0$                             | 42.6      | 13.3                                | 212  |
| Nano-defective Cu nanosheets                  | H-Cell                           | 0.1 M K <sub>2</sub> SO <sub>4</sub> | $-1.18$                            | 83.2      | $\sim 50$                           | 213  |
| Cu <sub>2</sub> O film                        | Teflon cell <sup>b</sup>         | 0.1 M KHCO <sub>3</sub>              | $-0.99$                            | 37.5      | 12.9                                | 214  |
| Cu mesocrystal                                | PTFE cell <sup>b</sup>           | 0.1 M KHCO <sub>3</sub>              | $-0.99$                            | 27.2      | 7                                   | 215  |
| B-doped Cu                                    | H-cell                           | 0.1 M KCl                            | $-1.1$                             | 52        | 36.4                                | 216  |
| Plasma treated Cu                             | H-cell                           | 0.1 M KHCO <sub>3</sub>              | $-1.0$                             | 45        | 15.3                                | 217  |
| <i>t</i> -Cu <sub>2</sub> O NPs/C             | H-cell                           | 0.1 M KHCO <sub>3</sub>              | $-1.1$                             | 59        | 24                                  | 218  |
| Cu <sub>2</sub> O NPs/C                       | H-cell                           | 0.1 M KHCO <sub>3</sub>              | $-1.1$                             | 57.3      | 12                                  | 219  |
| Cu <sub>3</sub> N nanocubes                   | H-cell                           | 0.1 M KHCO <sub>3</sub>              | $-1.6$                             | 60        | 18                                  | 220  |
| Pulsed-Cu                                     | H-cell                           | 0.1 M KHCO <sub>3</sub>              | $-1.0$                             | 48.6      | 20                                  | 221  |
| CuO <sub>x</sub>                              | H-cell                           | 0.1 M KHCO <sub>3</sub>              | $-1.3$                             | 53        | 14                                  | 222  |
| UiO-66-derived amorphous ZrO <sub>x</sub> /Cu | H-cell                           | 0.1 M KHCO <sub>3</sub>              | $-1.05$                            | 43.3      | 15.7                                | 223  |
| CuBr derived Cu nanodendrites                 | H-cell                           | 0.1 M KHCO <sub>3</sub>              | $-0.85$                            | $\sim 40$ | $\sim 9$                            | 224  |
| Cu on Cu <sub>3</sub> N                       | H-cell                           | 0.1 M KHCO <sub>3</sub>              | $-1.05$                            | 43        | $\sim 16.5$                         | 225  |
| Reconstructed Cu-I                            | H-cell                           | 0.1 M KHCO <sub>3</sub>              | $-1.09$                            | 59.9      | $\sim 15.7$                         | 226  |
| Cu <sub>1.8</sub> Se nanowires                | H-cell                           | 0.1 M KHCO <sub>3</sub>              | $-1.1$                             | 55        | 8.3                                 | 227  |
| A-Cu NWs                                      | H-cell                           | 0.1 M KHCO <sub>3</sub>              | $-1.0$                             | 69.79     | $\sim 18$                           | 228  |
| Cu/TiNT                                       | H-cell                           | 0.5 M KCl                            | $-1.6^c$                           | 55        | 132                                 | 229  |

<sup>a</sup> Potential at which maximum FE was obtained. <sup>b</sup> Custom made two compartment cell. <sup>c</sup> V vs. Ag/AgCl.

**Table 6** Examples of state-of-the-art Cu alloys and other Cu based catalysts that favour ethylene formation in flow/MEA cells

| Catalyst                    | Electrolysis cell configuration | Electrolyte             | Potential (V vs. RHE) <sup>a</sup> | FE (%) | $j_{\text{C}_2\text{H}_4}$ (mA cm <sup>-2</sup> ) | Ref. |
|-----------------------------|---------------------------------|-------------------------|------------------------------------|--------|---|------|
| Cu/ZnO                      | Plug flow reactor               | 1 M KOH                 | -0.9                               | ~50    | ~300  | 203  |
| CuAg nanowires              | Flow cell                       | 1 M KOH                 | -0.7                               | 60     | ~180  | 204  |
| Phase separated CuPd NPs    | Flow cell                       | 1 M KOH                 | -0.8                               | ~50    | ~180  | 64   |
| Ce doped Cu NPs             | Flow cell                       | 1 M KOH                 | -0.7                               | 53     | ~80   | 230  |
| Atomic Ni decorated Cu      | Flow cell                       | 1 M KOH                 | -0.88                              | 31.8   | 85  | 231  |
| Cu (100) nanocubes          | Flow cell                       | 1 M KOH                 | -0.7                               | 60     | 120   | 191  |
| Cu-DAT nanowires            | Flow cell                       | 1 M KOH                 | -0.6                               | 38.2   | 90  | 232  |
| Cu NPs                      | Flow cell                       | 1 M KOH                 | -0.58                              | 35     | 150   | 233  |
| Graphite/carbon NPs/Cu/PTFE | Flow cell                       | 7 M KOH                 | -0.55                              | 70     | ~70   | 234  |
| DVL-Cu                      | Flow cell                       | 1 M KCl                 | -0.81                              | 84.4   | 92.5  | 235  |
| Fluorinated-Cu              | Flow cell                       | 0.75 M KOH              | -0.89                              | 65     | 1040  | 236  |
| CuS/Cu-V                    | Flow cell                       | 1 M KOH                 | -0.92                              | 21.1   | 84  | 237  |
| Dendritic Cu                | Flow cell                       | 0.1 M KHCO <sub>3</sub> | -1.2                               | 36     | 162   | 238  |
| Nanoporous Cu               | Flow cell                       | 1 M KOH                 | -0.67                              | 38.6   | 252   | 239  |
| PTFE-Cu NPS                 | MEA                             | 0.1 M KHCO <sub>3</sub> | 3.8 <sup>b</sup>                   | 56.7   | 85  | 240  |
| Molecular tuned Cu          | MEA                             | 1 M KHCO <sub>3</sub>   | 3.65 <sup>b</sup>                  | 72     | 230   | 241  |
| Graphite/carbonNP/Cu/PTFE   | MEA                             | 1 M KHCO <sub>3</sub>   | 4.2 <sup>b</sup>                   | 46     | 92  | 242  |

<sup>a</sup> Potential at which maximum FE was obtained. <sup>b</sup> Cell voltage.

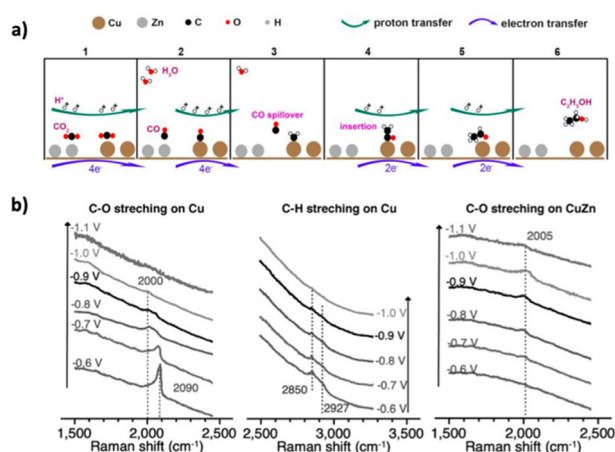


**Fig. 16** (a) Mechanism proposed for ethanol formation using CuZn catalysts. Reprinted with permission.<sup>243</sup> Copyright 2016, the American Chemical Society. (b) Operando Raman spectra obtained during electrolysis of saturated CO<sub>2</sub> in 0.1 M KHCO<sub>3</sub> solution using Cu and CuZn catalysts. Reprinted with permission.<sup>244</sup> Copyright 2019, Wiley-VCH Verlag GmbH & Co. KGaA, Weinheim.

were coated with ZnO (~30 nm thick) by atomic layer deposition. Subsequently, electrochemical reduction was undertaken to form a CuZn bimetallic layer (~90 nm) over the Cu nanorods. XRD analysis after electroreduction showed the presence of Cu and Zn/ZnO but not CuZn alloy. This CuZn catalyst was used to catalyze eCO<sub>2</sub>RR in 0.1 M KHCO<sub>3</sub> using an H-cell. Ethanol was produced at -1.15 V vs. RHE with a FE of 32% and a partial current density of 10.5 mA cm<sup>-2</sup>. The mechanism proposed in this study on the basis of analysis of Raman spectra (Fig. 16(b)) is similar to that suggested by Ren *et al.*<sup>243</sup> for the formation of ethanol using a phase segregated Cu<sub>x</sub>Zn catalyst.

An eCO<sub>2</sub>RR study by Lee *et al.*<sup>63</sup> also reveals the importance of Cu-Ag biphasic boundaries in achieving high ethanol

selectivity. The structure of this catalyst allows the CO concentration near the Cu-Ag phase blended catalyst surface to be increased, facilitating the insertion of CO into the Cu bound intermediates (\*CH<sub>2</sub>) to form \*COCH<sub>2</sub>. Upon further transfer of protons and electrons, \*COCH<sub>2</sub> is hydrogenated, resulting in the formation of ethanol *via* the acetaldehyde route. A recent eCO<sub>2</sub>RR study using CuO<sub>x</sub> coated Ag nanowires revealed an interesting relationship between the thickness of the CuO<sub>x</sub> layer and ethanol selectivity.<sup>245</sup> While the Ag/CuO<sub>x</sub>-y (core/shell-y, where y represents the average thickness of the shell in nm) samples with lower CuO<sub>x</sub> thickness (Ag/CuO<sub>x</sub>-10) showed substantial ethanol formation (Fig. 17(c)), ones with thicker CuO<sub>x</sub> favoured ethylene. *In situ* XAS studies (Fig. 17(d)) revealed that Ag/CuO<sub>x</sub>-10 initially contained Cu<sub>2</sub>O which was stable in the potential range of -0.5 to -0.7 V vs. RHE (Cu-O(Cu<sub>2</sub>O) and Cu-Cu(Cu<sub>2</sub>O) bands preserved) but reduced to Cu<sup>0</sup> at potentials more negative than -0.7 V resulting in formation of a Cu-Cu(Cu) bond (Cu-Cu band of metallic Cu). However, CuAg alloy was not formed during this reduction process. With Ag/CuO<sub>x</sub>-32, a less negative potential is sufficient to trigger this structural change. At a potential of -0.6 V vs. RHE, reduction of Cu<sub>2</sub>O to metallic Cu<sup>0</sup> was observed. Further, in both cases this led to a stable atomic arrangement in the potential range of -0.7 to -1.3 V vs. RHE resulting in enhanced C<sub>2</sub> product selectivity. The authors found that the existence of a majority of Cu in the +1 state facilitated the CO insertion mechanism and favoured ethanol production at Ag/CuO<sub>x</sub>-10 while the presence of more Cu<sup>0</sup> in Ag/CuO<sub>x</sub>-32 favoured C-C coupling mechanism which led to the formation of ethylene. This result signifies that the transformation of Cu (I) to Cu(0) is controlled by the CuO<sub>x</sub> thickness, which in turn influences the eCO<sub>2</sub>RR product selectivity.

Tables 7 and 8 summarise the state-of-the-art Cu alloys and other Cu based catalysts, which are selective for ethanol in H type and flow/membrane electrode assembly (MEA) cells, respectively.

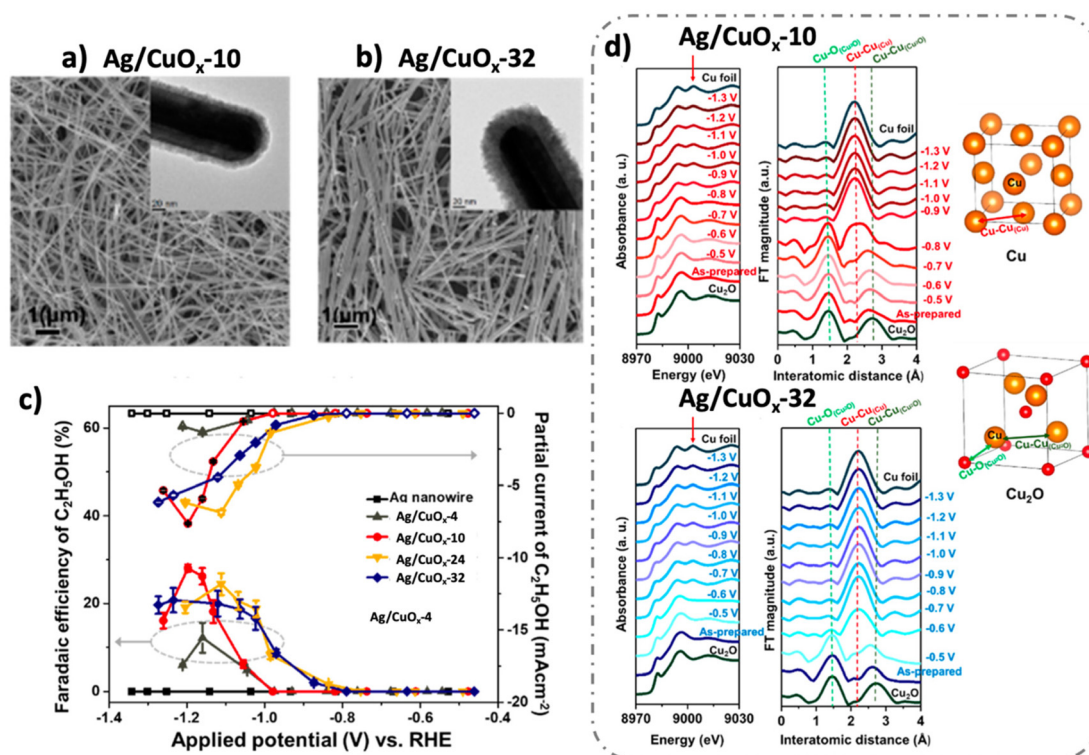


**Fig. 17** (a and b) SEM images of Ag/CuO<sub>x-y</sub> (core/shell-y, where y represents the average thickness of the shell in nm) catalysts, (c) ethanol faradaic efficiencies and partial current densities obtained with Ag/CuO<sub>x-y</sub> catalysts, (d) *in situ* XANES and EXAFS data obtained with Ag/CuO<sub>x-10</sub> and Ag/CuO<sub>x-32</sub> catalysts. Reprinted with permission.<sup>245</sup> Copyright 2019, the American Chemical Society. Source: <https://pubs.acs.org/doi/10.1021/acscentsci.9b01142>. Further permissions related to the material excerpted should be directed to the ACS.

**Table 7** Examples of state-of the art Cu alloy catalysts that favour ethanol production by eCO<sub>2</sub>RR in an H-cell

| Catalyst                                      | Electrolysis cell | Electrolyte             | Potential (V vs. RHE) <sup>a</sup> | FE (%) | <i>j</i> <sub>C<sub>2</sub>H<sub>5</sub>OH</sub> (mA cm <sup>-2</sup> ) | Ref. |
|---|-------------------|-------------------------|------------------------------------|--------|---|------|
| Cu <sub>4</sub> Zn                            | H-cell            | 0.1 M KHCO <sub>3</sub> | -1.05                              | 29     | 8.2   | 243  |
| CuO/ZnO                                       | PEEK <sup>b</sup> | 0.1 M KHCO <sub>3</sub> | -1.15                              | 32     | 10  | 244  |
| Ag/CuO <sub>x-10</sub>                        | H-cell            | 0.1 M KHCO <sub>3</sub> | -1.2                               | 29     | 7.6   | 245  |
| Cu <sub>3</sub> Sn                            | H-cell            | 0.1 M KHCO <sub>3</sub> | -1.0                               | 64     | 5.7   | 246  |
| Ag <sub>20</sub> Cu <sub>1</sub>              | H-cell            | 0.1 M KHCO <sub>3</sub> | -1.1                               | 16.5   | 4.1   | 247  |
| Au <sub>1</sub> Cu <sub>3</sub>               | H-cell            | 0.5 M KHCO <sub>3</sub> | -1.0                               | 29     | 5.6   | 248  |
| Cu <sub>5</sub> Zn <sub>8</sub>               | H-cell            | 0.1 M KHCO <sub>3</sub> | -0.8                               | 46.6   | 2.3   | 249  |
| Dendritic Cu-Cu <sub>2</sub> O                | H-cell            | 0.1 M KCl               | -0.4                               | 26     | 2.99  | 250  |
| CuO NPs                                       | H-cell            | 0.2 M KI                | -1.7 <sup>c</sup>                  | 36.1   | N.R   | 251  |
| Cu/carbon nanospire                           | H-cell            | 0.1 M KOH               | -1.2                               | 63     | ~3  | 252  |
| Cu-I  | H-cell            | 0.1 M KHCO <sub>3</sub> | -0.9                               | 25     | 11  | 253  |
| Cu-GNC-VL                                     | H-cell            | 0.5 M KHCO <sub>3</sub> | -0.9                               | 70.5   | 9   | 254  |
| Cu <sub>2</sub> /N <sub>0.14</sub> C          | H-cell            | 0.1 M KHCO <sub>3</sub> | -1.1                               | 51     | 14.4  | 255  |
| UiO-66-derived amorphous ZrO <sub>x</sub> /Cu | H-cell            | 0.1 M KHCO <sub>3</sub> | -1.1                               | 22.4   | 12.7  | 223  |
| Cu on Cu <sub>3</sub> N                       | H-cell            | 0.1 M KHCO <sub>3</sub> | -0.95                              | 18.4   | ~8  | 225  |
| Cu <sub>1.8</sub> Se nanowires                | H-cell            | 0.1 M KHCO <sub>3</sub> | -1.1                               | 24     | 3.5   | 227  |

N.R – not reported. <sup>a</sup> Potential at which maximum FE was obtained. <sup>b</sup> Custom made two compartment cell. <sup>c</sup> Potential (V) vs. SCE.

**4.3.3 Other C<sub>2</sub>/C<sub>2+</sub> products.** Apart from ethanol, acetate, propanol, and acetaldehyde are the other major oxygenates derived from CO<sub>2</sub> using the eCO<sub>2</sub>RR with copper containing electrocatalytic materials. However, despite significant efforts to enhance the yields of these other highly reduced products, faradaic efficiencies reported to date are still very low.

Acetate formation with reasonable selectivity (faradaic efficiency of 21% at -1.3 V vs. RHE), at 0 °C was achieved by the Meyer group by employing ultra-small (Cu)<sub>m</sub>(Ag)<sub>n</sub> (*m*, *n* denote the atomic ratios of Cu and Ag) bimetallic nanoparticles immobilised on a polymer. In 0.5 M KHCO<sub>3</sub> electrolyte containing 8 ppm benzotriazole at 0 °C, significant



**Table 8** Examples of state-of the art Cu alloy catalysts that favour ethanol production by eCO<sub>2</sub>RR in flow/MEA cells

| Catalyst                          | Electrolysis cell | Electrolyte             | Potential (V vs. RHE) <sup>a</sup> | FE (%) | $j_{C_2H_5OH}$ (mA cm <sup>-2</sup> ) | Ref. |
|-----------------------------------|-------------------|-------------------------|------------------------------------|--------|---------------------------------------|------|
| CuO/ZnO                           | Flow cell         | 1 M KOH                 | N.R                                | 41     | 82                                    | 244  |
| Phase separated CuPd NPs          | Flow cell         | 1 M KOH                 | -0.8                               | ~50    | ~180                                  | 64   |
| Cu <sub>2</sub> Zn <sub>1</sub>   | Flow cell         | 1 M KOH                 | -1.0                               | 26.2   | ~60                                   | 256  |
| CuAg nanowires                    | Flow cell         | 1 M KOH                 | -0.7                               | 25     | 75                                    | 204  |
| Binding-site diverse Ag/Cu        | Flow cell         | 1 M KOH                 | -0.67                              | 41     | 102                                   | 231  |
| Ag decorated Cu/Cu <sub>2</sub> O | Flow cell         | 1 M KOH                 | N.R                                | 19.2   | 304.5                                 | 257  |
| Atomic Ni decorated Cu            | Flow cell         | 1 M KOH                 | -0.88                              | 22.9   | 61.4                                  | 258  |
| N-C/Cu                            | Flow cell         | 1 M KOH                 | -0.68                              | 52     | 156                                   | 259  |
| Cu <sub>2</sub> O spheres         | Flow cell         | 2 M KOH                 | -0.61                              | 26.9   | 71.8                                  | 250  |
| Cu-DAT nanowires                  | Flow cell         | 1 M KOH                 | -0.69                              | 27.3   | ~35                                   | 232  |
| Fluorinated-Cu                    | Flow cell         | 2.5 M KOH               | -0.54                              | 16     | 128                                   | 236  |
| CuS/Cu-V                          | Flow cell         | 1 M KOH                 | -0.92                              | 24.7   | 99                                    | 237  |
| Nanoporous Cu                     | Flow cell         | 1 M KOH                 | -0.67                              | 16.6   | ~108                                  | 239  |
| Cu-DS                             | Flow cell         | 1 M KOH                 | -0.95                              | 52     | 52                                    | 260  |
| Cu <sub>2</sub> O NPs             | Flow cell         | 2 M KOH                 | -0.6                               | ~27    | 93                                    | 198  |
| FeTPP[Cl]/Cu                      | Flow cell         | 1 M KHCO <sub>3</sub>   | -0.82                              | 41     | 124                                   | 261  |
| FeTPP[Cl]/Cu                      | MEA               | 0.1 M KHCO <sub>3</sub> | 3.7 <sup>b</sup>                   | 45     | 100                                   | 261  |
| Cu <sub>3</sub> Sn                | MEA               | 1 M KOH                 | 3 <sup>b</sup>                     | 40     | 361                                   | 246  |
| PTFE-Cu NPS                       | MEA               | 0.1 M KHCO <sub>3</sub> | 4.2 <sup>b</sup>                   | 17.1   | ~40                                   | 240  |
| Graphite/carbonNP/Cu/PTFE         | MEA               | 0.1 M KHCO <sub>3</sub> | 4.2 <sup>b</sup>                   | ~15    | ~30                                   | 242  |
| Cu-DS                             | MEA               | 0.1 M KHCO <sub>3</sub> | 3.5 <sup>b</sup>                   | 50     | 95                                    | 260  |

N.R – not reported. <sup>a</sup> Potential at which maximum FE was obtained. <sup>b</sup> Cell voltage.

enhancement of acetate with a FE of 21.2% at -1.3 V vs. RHE was achieved on (Cu)<sub>m</sub>, (Ag)<sub>n</sub> compared to pure Cu where less than 1% of acetate was produced. The CO spillover mechanism from Ag to Cu was again proposed. As for ethanol production described above, CO inserted onto the Cu surface and then coupled with \*CH<sub>2</sub> to give the \*COCH<sub>2</sub> intermediate, but which in this case was further reduced to acetate *via* the acetaldehyde route. Since the availability of CO at copper is the limiting factor for C-C coupling, Lum *et al.*<sup>262</sup> have introduced sequential Cu-Au and Cu-Ag catalysts. These were microfabricated electrodes where Cu and Au or Ag were organized in a sequential order with predefined thickness of each metal and the distance between the two metals as shown in Fig. 18(a-c). In these catalysts, Cu is in close proximity with Au or Ag and favours formation of CO during eCO<sub>2</sub>RR. The generated CO spills over to the Cu surface and facilitates production of more highly reduced carbon fuels. By this strategy, these authors have improved the formation of oxygenate products to 41.3% which surpasses the selectivity of 26.1% achieved for hydrocarbons. The microfabricated Cu-Au or Cu-Ag electrodes used in these studies consisted of integrated but independent Cu and Au/Ag electrodes arranged adjacent to each other (Fig. 18(a-c)). As a result, the CO generated during eCO<sub>2</sub>RR was accumulated near adjacent Cu electrodes. By varying the distance between the Cu and Ag probes, the oxygenate to ethylene ratio can be varied from 0.5 to 2.4, with the highest faradaic efficiency of oxygenates reaching 41.4%, with total C<sub>2</sub>/C<sub>2+</sub> products being 65% (Fig. 18(d)). This study paves the way for new catalyst design strategies with controlled bimetallic arrangements for selective generation of C<sub>2</sub>/C<sub>2+</sub> products other than ethylene. Morales-Guio *et al.*<sup>263</sup> developed an Au/Cu tandem catalyst by depositing Au nanoparticles on Cu foil. This catalyst design provided more than a 100-fold increase in the rate of

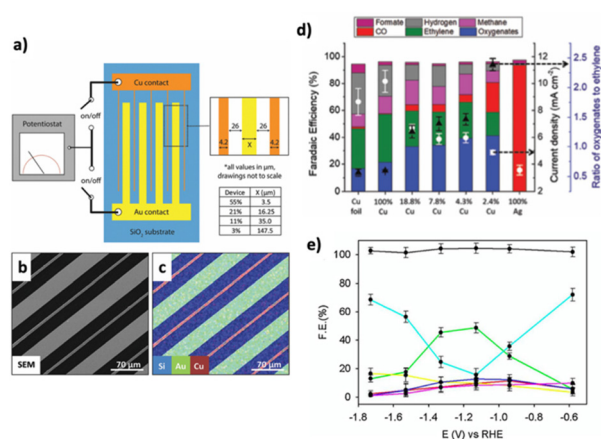


**Fig. 18** (a) Schematic diagram of a custom-made electrochemical device with microfabricated Au and Cu electrodes, (b) SEM and (c) EDX mapping of AuCu electrodes with 11% of geometric area occupied by Cu, (d) faradaic efficiencies and current densities obtained with AgCu electrodes. Reprinted with permission.<sup>262</sup> Copyright 2018, the Royal Society of Chemistry. (e) Faradaic efficiencies of products obtained with a Mo<sub>9</sub>/Cu heterostructure catalyst (cyan: hydrogen, red: ethanol, green: acetate, yellow: methane, blue: ethylene, purple: ethane). Reprinted with permission.<sup>264</sup> Copyright 2021, Elsevier B.V.

CO<sub>2</sub> reduction to the higher reduced carbon products. The improvement in C<sub>2</sub>/C<sub>2+</sub> alcohol production at low overpotentials was attributed to the enhanced local CO concentration provided by Au present in close proximity to copper.

Recently, the Wu group<sup>203</sup> have reported that enhancement in oxygenate production also can be achieved with a Cu/ZnO tandem catalyst. Tandem catalysts with variable ZnO loading were prepared by air brushing ZnO onto a Cu electrode pre-synthesised on a GDL electrode and dried under vacuum. By

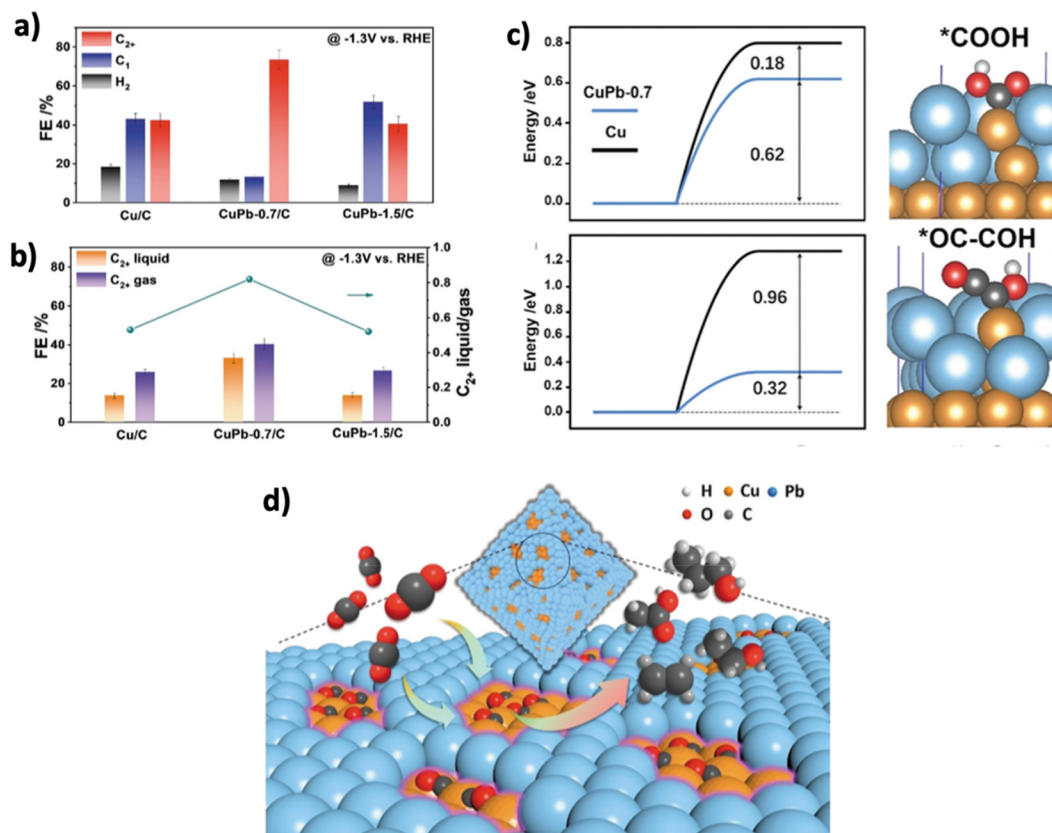


**Fig. 19** (a and b) Faradaic efficiencies of  $C_1$  and  $C_2$  products obtained using a CuPb-0.7/C (where 0.7 represents the thickness of Pb shell) catalyst, (c) simulated data and (d) schematic illustration of the production of  $C_{2+}$  products via the eCO<sub>2</sub>RR route. Reprinted with permission.<sup>265</sup> Copyright 2021, the American Chemical Society.

controlling the ZnO loading, effective spatial management of CO transport was achieved to optimise CO utilisation. High selectivity for  $C_{2+}$  products with a faradaic efficiency reaching 80% is achieved as shown in Fig. 14(e) with a partial current density of  $\sim 470 \text{ mA cm}^{-2}$  obtained with Cu<sub>1.0</sub>Zn<sub>0.2</sub>, values which respectively are 1.2 and 3.4 times higher than obtained with pure Cu.

An excellent conversion yield for CO<sub>2</sub> to acetate was reported recently at polyoxometalate modified Cu cubes. The Mo<sub>8</sub>/Cu

heterostructure catalyst was rich in Cu–O–Mo interfaces, which led to the generation of acetate with a FE of 48.8% at  $-1.13 \text{ V}$  (Fig. 18(e)) and a partial current density of  $68.9 \text{ mA cm}^{-2}$  in saturated NaHCO<sub>3</sub>.<sup>264</sup> The selectivity for  $C_{2+}$  products was found to be dependent on the thickness of the shell in Cu/Pb core/shell nanocubes. Cu/Pb nanocubes with an optimal shell thickness of 0.7 nm gave 73.5%  $C_{2+}$  products with a partial current density of  $294.4 \text{ mA cm}^{-2}$  at  $-1.3 \text{ V}$  in 1 M KOH solution under flow cell conditions (Fig. 19(a and b)).<sup>265</sup> DFT calculations

**Table 9** Examples of the state-of-the-art Cu alloys and other Cu based catalysts for other  $C_2/C_{2+}$  product formation with eCO<sub>2</sub>RR

| Catalyst                                  | Product                                    | Electrolysis cell              | Electrolyte                                   | Potential (V vs. RHE) <sup>a</sup> | FE (%)    | $j_{\text{product}}$ (mA cm <sup>-2</sup> ) | Ref. |
|---|--|--------------------------------|---|------------------------------------|-----------|---|------|
| (Cu) <sub>m</sub> , (Ag) <sub>n</sub> NPs | CH <sub>3</sub> COO <sup>-</sup>           | H-cell                         | 0.5 M KHCO <sub>3</sub> + 8 ppm benzotriazole | -1.33                              | 21        | N.R.  | 267  |
| Dendritic Cu–Cu <sub>2</sub> O            | CH <sub>3</sub> COO <sup>-</sup>           | H-cell                         | 0.1 M KCl                                     | -0.4                               | 40        | 4.6   | 250  |
| 4% Cu dots/Ag                             | Oxygenates                                 | PEEK <sup>b</sup>              | 0.1 M CsHCO <sub>3</sub>                      | -1.0                               | 41        | 4.4   | 262  |
| Mo <sub>8</sub> /Cu                       | CH <sub>3</sub> COO <sup>-</sup>           | Electrochemical batch cell     | Saturated NaHCO <sub>3</sub>                  | -1.13                              | 49        | 57  | 264  |
| CuBi                                      | C <sub>3</sub> H <sub>8</sub>              | Filter press cell              | 0.45 M KHCO <sub>3</sub> + 0.5 M KCl.         | N.R.                               | 85        | 38  | 266  |
| Single atom Cu/NPC                        | CH <sub>3</sub> COCH <sub>3</sub>          | H-cell                         | 0.1 M KHCO <sub>3</sub>                       | -0.36                              | 36.7      | N.R.  | 268  |
| CuI derived Cu nanofibres                 | C <sub>2</sub> H <sub>6</sub>              | H-cell                         | 0.1 M KHCO <sub>3</sub>                       | -0.73                              | $\sim 30$ | $\sim 9$                                    | 224  |
| CuS <sub>x</sub> -DSV                     | <i>n</i> -C <sub>3</sub> H <sub>7</sub> OH | H-cell                         | 0.1 M KHCO <sub>3</sub>                       | -1.05                              | 15.4      | $\sim 10$                                   | 269  |
| Graphene/ZnO/Cu <sub>2</sub> O            | <i>n</i> -C <sub>3</sub> H <sub>7</sub> OH | H-cell                         | 0.5 M NaHCO <sub>3</sub>                      | -0.9 <sup>c</sup>                  | 30        | N.R.  | 270  |
| MOF derived Cu                            | <i>n</i> -C <sub>3</sub> H <sub>7</sub> OH | Five port electrochemical cell | 0.1 M KHCO <sub>3</sub>                       | -2.4 <sup>c</sup>                  | $\sim 16$ | $\sim 4$                                    | 271  |

N.R. – not reported. <sup>a</sup> Potential at which maximum FE was obtained. <sup>b</sup> Custom made two compartment cell. <sup>c</sup> V vs. Ag/AgCl.

revealed that the synergistic effects due to the core/shell structure decreased the formation energies of \*COOH and \*OCCOH intermediates, thereby facilitating production of highly reduced carbon products as shown in Fig. 19(c and d). Azenha *et al.*<sup>266</sup> reported the production of propane with a remarkable FE of 84.6% by employing Bi coated CuO nanowires on a filter press cell in 1 M KOH. Bidentate carbonate formation on the catalyst surface was an important requirement for the formation of propane. Detailed investigations revealed that the presence of Cu(I) sites and oxygen defects influenced the binding affinity of CO<sub>2</sub> to the Bi/Cu NW catalyst in a manner which led to high selectivity for propane.

Table 9 summarises the state-of-the-art Cu alloys and other Cu based catalysts, which are selective for other C<sub>2</sub>/C<sub>2+</sub> products.

## 5. Conclusions and future directions

The development of rationally designed Cu based alloy catalysts is helping to address the problem of low product selectivity achieved by eCO<sub>2</sub>RR with pristine Cu. The reaction pathways can be manipulated by geometric and electronic effects that arise upon alloying a material. The choice of the guest elements alloyed with Cu and the spatial distribution of the constituent elements are crucial in determining the selectivity of eCO<sub>2</sub>RR products. In this review, the different strategies reported for alloying and their influence on the properties of the catalyst are surveyed. Achievements based on state-of-the-art Cu based alloy catalysts that improve the selectivity of the targeted product are highlighted.

Commonly, the selectivity of the product is related to the binding energies of key reaction intermediates which can be tuned by varying the structure of the alloy. For example, in alloys with ordered atomic structures, the elemental composition influences the bond length between the elements. This, in turn, influences the binding energies of eCO<sub>2</sub>RR intermediates adsorbed onto the catalyst surface, providing a systematic route to tuning product selectivity. On the other hand, a disordered alloy system can lead to changes in electronic and geometric structures during electrolysis which also influences the products that are formed. In the case of a core/shell type alloy structure, it is the strain and ligand effects, atomic vacancies and doping that affect the binding strength of reaction intermediates, again providing systematic routes to selectively tuning the product formation pathway. Phase separated alloys enhance the product selectivity in a unique way. In this class of alloy there is a clear separation in the phases of the different elements in the alloy, allowing each phase to individually generate the product that is characteristic of the element in the particular phase. Migration of products or the coupling of intermediates at the boundary of different phases is possible. This helps in producing highly reduced carbon products such as ethylene or ethanol with enhanced selectivity generally facilitated by the CO spillover mechanism.

Strategic alloying can introduce specific synergistic effects that are useful to tune the selectivity towards each product. However, other inevitably coupled effects could diminish the product selectivity. Hence, despite the ability to manipulate the reaction pathways by altering the binding energies, complete selectivity for one product remains exceedingly difficult to achieve when an alloying strategy is used alone. Therefore, integration with other catalyst design strategies is highly recommended.

Alloy structures also tend to be unstable under electrolysis conditions. The lifetime for most of the catalysts used to date is typically within a day, which is far less than that required for commercial applications. To address the problem of stability, high entropy alloys are now receiving considerable attention. These are a new class of alloy formed with multiple elements. HEAs are highly stable under extreme conditions, such as high temperatures and prolonged electrolysis conditions due to an exceptionally high kinetic solid diffusion barrier. They are active for eCO<sub>2</sub>RR, and in principle the electronic properties and hence selectivity can be precisely tuned as they possess exceptional flexibility for adjusting the binding energy compared to primitive alloys. HEAs consist of a minimum of five different elements, resulting in a wide range of compositions and atomic arrangements. Hence, powerful machine learning tools<sup>272,273</sup> are needed to identify the optimal composition and structure required to achieve selective generation of a desired eCO<sub>2</sub>RR product. Even though the suitable composition and structure of the HEAs are predicted theoretically, the currently used synthesis strategies for HEAs require high temperatures, pressures and an inert environment. Precisely controlling the microstructures or the local atomic arrangement also is highly complicated.<sup>274,275</sup>

The synergistic, so called “cocktail effect” displayed by HEAs with their multiple elemental combinations exhibit exceptional binding energies for reaction intermediates. The availability of different binding sites in these catalysts also can provide the possibility of wide range of binding energies for eCO<sub>2</sub>RR intermediates and thus provide the possibility to tune the selectivity of the products.<sup>274</sup> This property can be advantageous for cascade reactions, where the product formed at one binding site is desorbed from the surface and re-bound at the other for further reaction. Hence the choice of elements and atomic arrangement in the catalyst should be given priority when designing these catalysts. Copper based high entropy alloys are a focus as they provide the possibility of producing highly reduced hydrocarbon fuels with improved selectivity by means of cascade reactions. Support from theoretical studies is critical to extricate the full potential of such alloys.<sup>66,72,276</sup> Despite these highly attractive properties, application of HEAs in the eCO<sub>2</sub>RR is still limited.<sup>274,275</sup> Nellaippan *et al.*<sup>277</sup> achieved the first experimental realization of the application of nanocrystalline HEAs for eCO<sub>2</sub>RR. Nanocrystalline AuAgPtPdCu produces 100% of gaseous products including CO, CH<sub>4</sub> and C<sub>2</sub>H<sub>4</sub> at a low potential of -0.3 V vs. RHE with high hydrocarbon (CH<sub>4</sub> + C<sub>2</sub>H<sub>4</sub>) selectivity (~70%) in aqueous 0.5 M K<sub>2</sub>SO<sub>4</sub>. First principle based DFT calculations attribute this outcome to the destabilisation of

\*OCH<sub>3</sub> and highly enhanced stabilisation of \*O intermediates. Pedersen *et al.*<sup>66</sup> investigated the possibility of the formation of multicarbon products at HEAs by combining DFT with machine learning with (111) facets of CoCuGaNiZn and AgAuCuPdPt as model systems. The authors established a correlation between composition and the variation in H and CO binding energies.

In addition to achieving a more rational design of catalyst material, understanding the mechanism of eCO<sub>2</sub>RR at the atomic level should make it possible to establish more precise structure–property relationships. From this perspective, advanced *in situ* characterisation techniques are receiving increased attention.<sup>278–280</sup> Several studies have shown that mixed oxidation states of Cu stabilise reaction intermediates that produce highly reduced C<sub>2</sub> fuels.<sup>43,65,198,210,281</sup> However, recent *in situ* studies through a combination of synchrotron based grazing incidence X-ray absorption and X-ray diffraction spectroscopy have suggested that Cu is present in the metallic 0 oxidation state during electrolysis.<sup>200</sup> Such contradictory results may be due to structural differences in the catalytic materials. Clearly, morphological and structural changes in the catalyst during electrolysis need to be monitored. Development of more sensitive *in situ* spectroscopic and microscopic structural characterisation tools is needed.

Finally, the electrolysis system design must be optimised to enhance mass transport rates for both reactants and products. Recent research has demonstrated that use of gas diffusion electrodes and membrane electrode assemblies allow current densities to be increased drastically compared to those achievable with conventional H-shaped electrolysis cells.<sup>234,282,283</sup> Improved cell designs and reaction conditions that allow much higher current densities, lower resistance and higher stability are essential to reach commercially viable efficiencies. So far, high purity CO<sub>2</sub> gas has been commonly used in eCO<sub>2</sub>RR studies. To fully realize the potential of the eCO<sub>2</sub>RR for commercial application, the effect of impurities, such as SO<sub>x</sub>, NO<sub>x</sub>, which are commonly present in the industrial flue gases, should be investigated. However, research towards this direction is still limited.<sup>284</sup>

In summary, eCO<sub>2</sub>RR is a viable method for utilising CO<sub>2</sub>. However, even though eCO<sub>2</sub>RR can produce a variety of commercially valuable fuels, manufacturing of targeted products with high selectivity remains difficult. Using catalysts derived from alloying with Cu addresses some of the limitations since it allows considerable control over product selectivity by changing the guest element and the alloy structure. Despite many significant achievements emerging from the development of efficient Cu based alloy catalysts, fabrication of catalysts that have high stability and can generate significantly reduced carbon products in commercially viable quantities at competitive prices remains highly challenging.

## Conflicts of interest

There are no conflicts to declare.

## Acknowledgements

The authors thank the Australian Research Council for financial support though the ARC Centre of Excellence for Electromaterials Science.

## References

- 1 R. B. Jackson, C. Le Quéré, R. M. Andrew, J. G. Canadell, G. P. Peters, J. Roy and L. Wu, *Environ. Res. Lett.*, 2017, **12**, 110202.
- 2 Carbon dioxide peaks near 420 parts per million at Mauna Loa observatory, <https://research.noaa.gov/article/ArtMID/587/ArticleID/2742/Despite-pandemic-shutdowns-carbon-dioxide-and-methane-surged-in-2020>, <https://research.noaa.gov/article/ArtMID/587/ArticleID/2764/Coronavirus-response-barely-slows-rising-carbon-dioxide>, (accessed 10.05.2022, <https://research.noaa.gov/article/ArtMID/587/ArticleID/2764/Coronavirus-response-barely-slows-rising-carbon-dioxide>).
- 3 I. Sullivan, A. Goryachev, I. A. Digdaya, X. Li, H. A. Atwater, D. A. Vermaas and C. Xiang, *Nat. Catal.*, 2021, **4**, 952–958.
- 4 J. Albero, Y. Peng and H. García, *ACS Catal.*, 2020, **10**, 5734–5749.
- 5 A. Hezam, K. Namratha, Q. A. Drmash, D. Ponnamma, J. Wang, S. Prasad, M. Ahamed, C. Cheng and K. Byrappa, *ACS Appl. Nano Mater.*, 2020, **3**, 138–148.
- 6 Z. Hu and W. Liu, *ACS Appl. Mater. Interfaces*, 2020, **12**, 51366–51373.
- 7 J. Ran, M. Jaroniec and S.-Z. Qiao, *Adv. Mater.*, 2018, **30**, 1704649.
- 8 F. L. Sousa, M. Preiner and W. F. Martin, *Curr. Opin. Microbiol.*, 2018, **43**, 77–83.
- 9 A. M. Appel, J. E. Bercaw, A. B. Bocarsly, H. Dobbek, D. L. DuBois, M. Dupuis, J. G. Ferry, E. Fujita, R. Hille, P. J. A. Kenis, C. A. Kerfeld, R. H. Morris, C. H. F. Peden, A. R. Portis, S. W. Ragsdale, T. B. Rauchfuss, J. N. H. Reek, L. C. Seefeldt, R. K. Thauer and G. L. Waldrop, *Chem. Rev.*, 2013, **113**, 6621–6658.
- 10 D. Dong, P. Aleta, X. Zhao, O. K. Choi, S. Kim and J. W. Lee, *Bioresour. Technol.*, 2019, **275**, 314–320.
- 11 S. Roy, A. Cherevotan and S. C. Peter, *ACS Energy Lett.*, 2018, **3**, 1938–1966.
- 12 E. Sediva, A. J. Carrillo, C. E. Halloran and J. L. M. Rupp, *ACS Appl. Energy Mater.*, 2021, **4**, 1474–1483.
- 13 R. R. Bhosale, G. Takalkar, P. Sutar, A. Kumar, F. AlMomani and M. Khraisheh, *Int. J. Hydrogen Energy*, 2019, **44**, 34–60.
- 14 X. Chang, T. Wang and J. Gong, *Energy Environ. Sci.*, 2016, **9**, 2177–2196.
- 15 S. Roy and S. C. Peter, in *Advances in the Chemistry and Physics of Materials*, 2019, pp. 399–428, DOI: [10.1142/9789811211331\\_0017](https://doi.org/10.1142/9789811211331_0017).

- 16 P. R. Yaashikaa, P. S. Kumar, S. J. Varjani and A. Saravanan, *J. CO2 Util.*, 2019, **33**, 131–147.
- 17 S. Nitopi, E. Bertheussen, S. B. Scott, X. Liu, A. K. Engstfeld, S. Horch, B. Seger, I. E. L. Stephens, K. Chan, C. Hahn, J. K. Nørskov, T. F. Jaramillo and I. Chorkendorff, *Chem. Rev.*, 2019, **119**, 7610–7672.
- 18 J. Resasco, L. D. Chen, E. Clark, C. Tsai, C. Hahn, T. F. Jaramillo, K. Chan and A. T. Bell, *J. Am. Chem. Soc.*, 2017, **139**, 11277–11287.
- 19 Y. Lum, B. Yue, P. Lobaccaro, A. T. Bell and J. W. Ager, *J. Phys. Chem. C*, 2017, **121**, 14191–14203.
- 20 J. Resasco, Y. Lum, E. Clark, J. Z. Zeddon and A. T. Bell, *ChemElectroChem*, 2018, **5**, 1064–1072.
- 21 J. E. Pander III, D. Ren, Y. Huang, N. W. X. Loo, S. H. L. Hong and B. S. Yeo, *ChemElectroChem*, 2018, **5**, 219–237.
- 22 M. König, J. Vaes, E. Klemm and D. Pant, *iScience*, 2019, **19**, 135–160.
- 23 A. Wagner, C. D. Sahm and E. Reisner, *Nat. Catal.*, 2020, **3**, 775–786.
- 24 E. R. Corson, E. B. Creel, R. Kostecki, J. J. Urban and B. D. McCloskey, *Electrochim. Acta*, 2021, **374**, 137820.
- 25 A. Vasileff, C. Xu, Y. Jiao, Y. Zheng and S.-Z. Qiao, *Chem*, 2018, **4**, 1809–1831.
- 26 F. Li, L. Chen, G. P. Knowles, D. R. MacFarlane and J. Zhang, *Angew. Chem., Int. Ed.*, 2017, **56**, 505–509.
- 27 T. Burdyny and W. A. Smith, *Energy Environ. Sci.*, 2019, **12**, 1442–1453.
- 28 C.-T. Dinh, T. Burdyny, M. G. Kibria, A. Seifitokaldani, C. M. Gabardo, F. P. García de Arquer, A. Kiani, J. P. Edwards, P. De Luna, O. S. Bushuyev, C. Zou, R. Quintero-Bermudez, Y. Pang, D. Sinton and E. H. Sargent, *Science*, 2018, **360**, 783–787.
- 29 C.-T. Dinh, F. P. García de Arquer, D. Sinton and E. H. Sargent, *ACS Energy Lett.*, 2018, **3**, 2835–2840.
- 30 D. M. Weekes, D. A. Salvatore, A. Reyes, A. Huang and C. P. Berlinguette, *Acc. Chem. Res.*, 2018, **51**, 910.
- 31 D. Higgins, C. Hahn, C. Xiang, T. F. Jaramillo and A. Z. Weber, *ACS Energy Lett.*, 2019, **4**, 317.
- 32 K. Liu, W. A. Smith and T. Burdyny, *ACS Energy Lett.*, 2019, **4**, 639–643.
- 33 C. Delacourt, P. L. Ridgway, J. B. Kerr and J. Newman, *J. Electrochem. Soc.*, 2008, **155**, B42.
- 34 L. M. Aeshala, R. Uppaluri and A. Verma, *Phys. Chem. Chem. Phys.*, 2014, **16**, 17588–17594.
- 35 N. Gutiérrez-Guerra, L. Moreno-López, J. C. Serrano-Ruiz, J. L. Valverde and A. de Lucas-Consuegra, *Appl. Catal., B*, 2016, **188**, 272–282.
- 36 C. Xiao and J. Zhang, *ACS Nano*, 2021, **15**, 7975–8000.
- 37 M. B. Ross, P. De Luna, Y. Li, C.-T. Dinh, D. Kim, P. Yang and E. H. Sargent, *Nat. Catal.*, 2019, **2**, 648–658.
- 38 K. P. Kuhl, E. R. Cave, D. N. Abram and T. F. Jaramillo, *Energy Environ. Sci.*, 2012, **5**, 7050–7059.
- 39 A. S. Varela, W. Ju, T. Reier and P. Strasser, *ACS Catal.*, 2016, **6**, 2136–2144.
- 40 A. A. Peterson, F. Abild-Pedersen, F. Studt, J. Rossmeisl and J. K. Nørskov, *Energy Environ. Sci.*, 2010, **3**, 1311–1315.
- 41 Y. Hori, I. Takahashi, O. Koga and N. Hoshi, *J. Phys. Chem. B*, 2002, **106**, 15–17.
- 42 B. Zhang, B. Zhang, Y. Jiang, T. Ma, H. Pan and W. Sun, *Small*, 2021, **17**, 2101443.
- 43 G. M. Tomboc, S. Choi, T. Kwon, Y. J. Hwang and K. Lee, *Adv. Mater.*, 2020, **32**, 1908398.
- 44 A. R. Woldu, Z. Huang, P. Zhao, L. Hu and D. Astruc, *Coord. Chem. Rev.*, 2022, **454**, 214340.
- 45 C. E. Creissen and M. Fontecave, *Nat. Commun.*, 2022, **13**, 2280.
- 46 C. Cao and Z. Wen, *J. CO2 Util.*, 2017, **22**, 231–237.
- 47 P. Huang, S. Ci, G. Wang, J. Jia, J. Xu and Z. Wen, *J. CO2 Util.*, 2017, **20**, 27–33.
- 48 P. Shao, S. Ci, L. Yi, P. Cai, P. Huang, C. Cao and Z. Wen, *ChemElectroChem*, 2017, **4**, 2593–2598.
- 49 J. Jia, X. Hao, Y. Chang, M. Jia and Z. Wen, *J. Colloid Interface Sci.*, 2021, **586**, 491–497.
- 50 J. He, N. J. J. Johnson, A. Huang and C. P. Berlinguette, *ChemSusChem*, 2018, **11**, 48–57.
- 51 C. Kim, F. Dionigi, V. Beermann, X. Wang, T. Möller and P. Strasser, *Adv. Mater.*, 2019, **31**, 1805617.
- 52 Y. Jia, F. Li, K. Fan and L. Sun, *Adv. Powder Technol.*, 2022, **1**, 100012.
- 53 G. Wang, J. Chen, Y. Ding, P. Cai, L. Yi, Y. Li, C. Tu, Y. Hou, Z. Wen and L. Dai, *Chem. Soc. Rev.*, 2021, **50**, 4993–5061.
- 54 P. Devi, R. Verma and J. P. Singh, *J. CO2 Util.*, 2022, **65**, 102211.
- 55 M. Watanabe, M. Shibata, A. Kato, M. Azuma and T. Sakata, *J. Electrochem. Soc.*, 1991, **138**, 3382–3389.
- 56 V. Ponc, *Appl. Catal., A*, 2001, **222**, 31–45.
- 57 L. Xie, J. Liang, C. Priest, T. Wang, D. Ding, G. Wu and Q. Li, *Chem. Commun.*, 2021, **57**, 1839–1854.
- 58 H. Y. Kim and S. H. Joo, *J. Mater. Chem. A*, 2020, **8**, 8195–8217.
- 59 A. Groß, *Top. Catal.*, 2006, **37**, 29–39.
- 60 A. Schlapka, M. Lischka, A. Groß, U. Käsberger and P. Jakob, *Phys. Rev. Lett.*, 2003, **91**, 016101.
- 61 Y. Gauthier, M. Schmid, S. Padovani, E. Lundgren, V. Buš, G. Kresse, J. Redinger and P. Varga, *Phys. Rev. Lett.*, 2001, **87**, 036103.
- 62 K. Sun, T. Cheng, L. Wu, Y. Hu, J. Zhou, A. Maclennan, Z. Jiang, Y. Gao, W. A. Goddard and Z. Wang, *J. Am. Chem. Soc.*, 2017, **139**, 15608–15611.
- 63 S. Lee, G. Park and J. Lee, *ACS Catal.*, 2017, **7**, 8594–8604.
- 64 S. Ma, M. Sadakiyo, M. Heima, R. Luo, R. T. Haasch, J. I. Gold, M. Yamauchi and P. J. A. Kenis, *J. Am. Chem. Soc.*, 2017, **139**, 47–50.
- 65 V. S. S. Mosali, X. Zhang, Y. Liang, L. Li, G. Puxty, M. D. Horne, A. Brajter-Toth, A. M. Bond and J. Zhang, *ChemSusChem*, 2021, **14**, 2924–2934.
- 66 J. K. Pedersen, T. A. A. Batchelor, A. Bagger and J. Rossmeisl, *ACS Catal.*, 2020, **10**, 2169–2176.

- 67 X. Wang, W. Guo and Y. Fu, *J. Mater. Chem. A*, 2021, **9**, 663–701.
- 68 Y. Zhang, D. Wang and S. Wang, *Small*, 2022, **18**, 2104339.
- 69 K. Y. Tsai, M. H. Tsai and J. W. Yeh, *Acta Mater.*, 2013, **61**, 4887–4897.
- 70 Y. Zhang, T. T. Zuo, Z. Tang, M. C. Gao, K. A. Dahmen, P. K. Liaw and Z. P. Lu, *Prog. Mater. Sci.*, 2014, **61**, 1–93.
- 71 S. Chen, H. S. Oh, B. Gludovatz, S. J. Kim, E. S. Park, Z. Zhang, R. O. Ritchie and Q. Yu, *Nat. Commun.*, 2020, **11**, 826.
- 72 T. Löffler, A. Ludwig, J. Rossmeisl and W. Schuhmann, *Angew. Chem., Int. Ed.*, 2021, **60**, 26894–26903.
- 73 W. Zhang, C. Xu, Y. Hu, S. Yang, L. Ma, L. Wang, P. Zhao, C. Wang, J. Ma and Z. Jin, *Nano Energy*, 2020, **73**, 104796.
- 74 Y.-X. Duan, K.-H. Liu, Q. Zhang, J.-M. Yan and Q. Jiang, *Small Methods*, 2020, **4**, 1900846.
- 75 W. Zhang, Y. Hu, L. Ma, G. Zhu, P. Zhao, X. Xue, R. Chen, S. Yang, J. Ma, J. Liu and Z. Jin, *Nano Energy*, 2018, **53**, 808–816.
- 76 M. Zhao, Y. Gu, W. Gao, P. Cui, H. Tang, X. Wei, H. Zhu, G. Li, S. Yan, X. Zhang and Z. Zou, *Appl. Catal., B*, 2020, **266**, 118625.
- 77 P. Su, W. Xu, Y. Qiu, T. Zhang, X. Li and H. Zhang, *ChemSusChem*, 2018, **11**, 848–853.
- 78 W. Zhang, S. Yang, M. Jiang, Y. Hu, C. Hu, X. Zhang and Z. Jin, *Nano Lett.*, 2021, **21**, 2650–2657.
- 79 J. Huang, X. Guo, Y. Wei, Q. Hu, X. Yu and L. Wang, *J. CO<sub>2</sub> Util.*, 2019, **33**, 166–170.
- 80 Y. Chen and M. W. Kanan, *J. Am. Chem. Soc.*, 2012, **134**, 1986–1989.
- 81 F. Cheng, X. Zhang, K. Mu, X. Ma, M. Jiao, Z. Wang, P. Limpachanangkul, B. Chalermisinsuwan, Y. Gao, Y. Li, Z. Chen and L. Liu, *Energy Technol.*, 2021, **9**, 2000799.
- 82 F. Li, L. Chen, M. Xue, T. Williams, Y. Zhang, D. R. MacFarlane and J. Zhang, *Nano Energy*, 2017, **31**, 270–277.
- 83 J. Gu, F. Héroguel, J. Luterbacher and X. Hu, *Angew. Chem., Int. Ed.*, 2018, **57**, 2943–2947.
- 84 J. Huang, X. Guo, X. Huang and L. Wang, *Electrochim. Acta*, 2019, **325**, 134923.
- 85 X. Huang, J. Song, H. Wu, C. Xie, M. Hua, Y. Hu and B. Han, *ChemSusChem*, 2020, **13**, 6346–6352.
- 86 S. Back, J.-H. Kim, Y.-T. Kim and Y. Jung, *Phys. Chem. Chem. Phys.*, 2016, **18**, 9652–9657.
- 87 Y. Wang, J. Liu, Y. Wang, A. M. Al-Enizi and G. Zheng, *Small*, 2017, **13**, 1701809.
- 88 V. S. K. Yadav and M. K. Purkait, *RSC Adv.*, 2015, **5**, 40414–40421.
- 89 D. Gao, H. Zhou, F. Cai, J. Wang, G. Wang and X. Bao, *ACS Catal.*, 2018, **8**, 1510–1519.
- 90 B. Jiang, X.-G. Zhang, K. Jiang, D.-Y. Wu and W.-B. Cai, *J. Am. Chem. Soc.*, 2018, **140**, 2880–2889.
- 91 F. Cai, D. Gao, H. Zhou, G. Wang, T. He, H. Gong, S. Miao, F. Yang, J. Wang and X. Bao, *Chem. Sci.*, 2017, **8**, 2569–2573.
- 92 T.-W. Jiang, Y.-W. Zhou, X.-Y. Ma, X. Qin, H. Li, C. Ding, B. Jiang, K. Jiang and W.-B. Cai, *ACS Catal.*, 2021, **11**, 840–848.
- 93 F. Zhou, H. Li, M. Fournier and D. R. MacFarlane, *ChemSusChem*, 2017, **10**, 1509–1516.
- 94 P. Huang, M. Cheng, H. Zhang, M. Zuo, C. Xiao and Y. Xie, *Nano Energy*, 2019, **61**, 428–434.
- 95 F. Li, M. Xue, J. Li, X. Ma, L. Chen, X. Zhang, D. R. MacFarlane and J. Zhang, *Angew. Chem., Int. Ed.*, 2017, **56**, 14718–14722.
- 96 Z. Jiang, T. Wang, J. Pei, H. Shang, D. Zhou, H. Li, J. Dong, Y. Wang, R. Cao, Z. Zhuang, W. Chen, D. Wang, J. Zhang and Y. Li, *Energy Environ. Sci.*, 2020, **13**, 2856–2863.
- 97 N. Han, P. Ding, L. He, Y. Li and Y. Li, *Adv. Energy Mater.*, 2020, **10**, 1902338.
- 98 Q. Li, X. Zhang, X. Zhou, Q. Li, H. Wang, J. Yi, Y. Liu and J. Zhang, *J. CO<sub>2</sub> Util.*, 2020, **37**, 106–112.
- 99 V. S. S. Mosali, X. Zhang, Y. Zhang, T. Gengenbach, S.-X. Guo, G. Puxty, M. D. Horne, A. M. Bond and J. Zhang, *ACS Sustainable Chem. Eng.*, 2019, **7**, 19453–19462.
- 100 K. Ohkawa, Y. Noguchi, S. Nakayama, K. Hashimoto and A. Fujishima, *J. Electroanal. Chem.*, 1993, **348**, 459–464.
- 101 K. Ohkawa, Y. Noguchi, S. Nakayama, K. Hashimoto and A. Fujishima, *J. Electroanal. Chem.*, 1994, **367**, 165–173.
- 102 X. Zhang, F. Li, Y. Zhang, A. M. Bond and J. Zhang, *J. Mater. Chem. A*, 2018, **6**, 7851–7858.
- 103 W. He, I. Liberman, I. Rozenberg, R. Ifraemov and I. Hod, *Angew. Chem., Int. Ed.*, 2020, **59**, 8262–8269.
- 104 Y. Hori, in *Modern Aspects of Electrochemistry*, ed. C. Vayenas, Springer, New York, 2008, vol. 42, ch. 3, p. 89.
- 105 M. Zhao, H. Tang, Q. Yang, Y. Gu, H. Zhu, S. Yan and Z. Zou, *ACS Appl. Mater. Interfaces*, 2020, **12**, 4565–4571.
- 106 M. Morimoto, Y. Takatsuji, K. Hirata, T. Fukuma, T. Ohno, T. Sakakura and T. Haruyama, *Electrochim. Acta*, 2018, **290**, 255–261.
- 107 J. Rosen, G. S. Hutchings, Q. Lu, R. V. Forest, A. Moore and F. Jiao, *ACS Catal.*, 2015, **5**, 4586–4591.
- 108 T. Zhang, X. Li, Y. Qiu, P. Su, W. Xu, H. Zhong and H. Zhang, *J. Catal.*, 2018, **357**, 154–162.
- 109 W. Luo, J. Zhang, M. Li and A. Züttel, *ACS Catal.*, 2019, **9**, 3783–3791.
- 110 D. Sun, X. Xu, Y. Qin, S. P. Jiang and Z. Shao, *ChemSusChem*, 2020, **13**, 39–58.
- 111 M. Ma, K. Liu, J. Shen, R. Kas and W. A. Smith, *ACS Energy Lett.*, 2018, **3**, 1301–1306.
- 112 S. Y. Chae, S. Y. Lee and O.-S. Joo, *Electrochim. Acta*, 2019, **303**, 118–124.
- 113 S. A. Mahyoub, F. A. Qaraah, C. Chen, F. Zhang, S. Yan and Z. Cheng, *Sustainable Energy Fuels*, 2020, **4**, 50–67.
- 114 X. Peng, S. G. Karakalos and W. E. Mustain, *ACS Appl. Mater. Interfaces*, 2018, **10**, 1734–1742.
- 115 S. Chen and A. Chen, *J. Phys. Chem. C*, 2019, **123**, 23898–23906.

- 116 Y. Fang and J. C. Flake, *J. Am. Chem. Soc.*, 2017, **139**, 3399–3405.
- 117 H.-E. Lee, K. D. Yang, S. M. Yoon, H.-Y. Ahn, Y. Y. Lee, H. Chang, D. H. Jeong, Y.-S. Lee, M. Y. Kim and K. T. Nam, *ACS Nano*, 2015, **9**, 8384–8393.
- 118 J. A. Trindell, J. Clausmeyer and R. M. Crooks, *J. Am. Chem. Soc.*, 2017, **139**, 16161–16167.
- 119 S. Mezzavilla, S. Horch, I. E. L. Stephens, B. Seger and I. Chorkendorff, *Angew. Chem., Int. Ed.*, 2019, **58**, 3774–3778.
- 120 Y. Zhao, X. Tan, W. Yang, C. Jia, X. Chen, W. Ren, S. C. Smith and C. Zhao, *Angew. Chem., Int. Ed.*, 2020, **59**, 21493–21498.
- 121 W. Zhu, S. Kattel, F. Jiao and J. G. Chen, *Adv. Energy Mater.*, 2019, **9**, 1802840.
- 122 H. Dong, L. Zhang, P. Yang, X. Chang, W. Zhu, X. Ren, Z.-J. Zhao and J. Gong, *Chem. Eng. Sci.*, 2019, **194**, 29–35.
- 123 Z. Han, C. Choi, H. Tao, Q. Fan, Y. Gao, S. Liu, A. W. Robertson, S. Hong, Y. Jung and Z. Sun, *Catal. Sci. Technol.*, 2018, **8**, 3894–3900.
- 124 R. Hegner, L. F. M. Rosa and F. Harnisch, *Appl. Catal., B*, 2018, **238**, 546–556.
- 125 Z. Xia, M. Freeman, D. Zhang, B. Yang, L. Lei, Z. Li and Y. Hou, *ChemElectroChem*, 2018, **5**, 253–259.
- 126 W. Yang, Y. Zhao, S. Chen, W. Ren, X. Chen, C. Jia, Z. Su, Y. Wang and C. Zhao, *Inorg. Chem.*, 2020, **59**, 12437–12444.
- 127 K. Mou, Z. Chen, S. Yao and L. Liu, *Electrochim. Acta*, 2018, **289**, 65–71.
- 128 P. Lu, X. Tan, H. Zhao, Q. Xiang, K. Liu, X. Zhao, X. Yin, X. Li, X. Hai, S. Xi, A. T. S. Wee, S. J. Pennycook, X. Yu, M. Yuan, J. Wu, G. Zhang, S. C. Smith and Z. Yin, *ACS Nano*, 2021, **15**, 5671–5678.
- 129 D. H. Won, C. H. Choi, J. Chung, M. W. Chung, E.-H. Kim and S. I. Woo, *ChemSusChem*, 2015, **8**, 3092–3098.
- 130 S. Zhang, P. Kang and T. J. Meyer, *J. Am. Chem. Soc.*, 2014, **136**, 1734–1737.
- 131 Y. Wang, C. Niu and D. Wang, *J. Colloid Interface Sci.*, 2018, **527**, 95–106.
- 132 X. An, S. Li, A. Yoshida, Z. Wang, X. Hao, A. Abudula and G. Guan, *ACS Sustainable Chem. Eng.*, 2019, **7**, 9360–9368.
- 133 Y. Zhang, L. Chen, F. Li, C. D. Easton, J. Li, A. M. Bond and J. Zhang, *ACS Catal.*, 2017, **7**, 4846–4853.
- 134 A. Katoh, H. Uchida, M. Shibata and M. Watanabe, *J. Electrochem. Soc.*, 1994, **141**, 2054–2058.
- 135 J. He, K. E. Dettelbach, A. Huang and C. P. Berlinguette, *Angew. Chem., Int. Ed.*, 2017, **56**, 16579–16582.
- 136 D. Li, L. Huang, Y. Tian, T. Liu, L. Zhen and Y. Feng, *Appl. Catal., B*, 2021, **292**, 120119.
- 137 Y. Xiong, B. Wei, M. Wu, B. Hu, F. Zhu, J. Hao and W. Shi, *J. CO<sub>2</sub> Util.*, 2021, **51**, 101621.
- 138 Z. Tao, Z. Wu, X. Yuan, Y. Wu and H. Wang, *ACS Catal.*, 2019, **9**, 10894–10898.
- 139 X. Jiang, X. Wang, Z. Liu, Q. Wang, X. Xiao, H. Pan, M. Li, J. Wang, Y. Shao, Z. Peng, Y. Shen and M. Wang, *Appl. Catal., B*, 2019, **259**, 118040.
- 140 C. Chen, Y. Pang, F. Zhang, J. Zhong, B. Zhang and Z. Cheng, *J. Mater. Chem. A*, 2018, **6**, 19621–19630.
- 141 M. Zhang, Z. Zhang, Z. Zhao, H. Huang, D. H. Anjum, D. Wang, J.-h. He and K.-W. Huang, *ACS Catal.*, 2021, **11**, 11103–11108.
- 142 Q. Xie, G. O. Larrazábal, M. Ma, I. Chorkendorff, B. Seger and J. Luo, *J. Energy Chem.*, 2021, **63**, 278–284.
- 143 Z. Yang, H. Wang, X. Fei, W. Wang, Y. Zhao, X. Wang, X. Tan, Q. Zhao, H. Wang, J. Zhu, L. Zhou, H. Ning and M. Wu, *Appl. Catal., B*, 2021, **298**, 120571.
- 144 A. W. Kahsay, K. B. Ibrahim, M.-C. Tsai, M. K. Birhanu, S. A. Chala, W.-N. Su and B.-J. Hwang, *Catal. Lett.*, 2019, **149**, 860–869.
- 145 Z. Zhang, W. Liu, W. Zhang, M. Liu and S. Huo, *Colloids Surf., A*, 2021, **631**, 127637.
- 146 T. Shinagawa, G. O. Larrazábal, A. J. Martín, F. Krumeich and J. Pérez-Ramírez, *ACS Catal.*, 2018, **8**, 837–844.
- 147 J. Du, Y. Xin, M. Dong, J. Yang, Q. Xu, H. Liu and B. Han, *Small*, 2021, **17**, 2102629.
- 148 Y. Huang, Y. Deng, A. D. Handoko, G. K. L. Goh and B. S. Yeo, *ChemSusChem*, 2018, **11**, 320–326.
- 149 Y. Wang, Y. Chen, Y. Zhao, J. Yu, Z. Liu, Y. Shi, H. Liu, X. Li and W. Zhou, *Appl. Catal., B*, 2022, **307**, 120991.
- 150 J. Lim, A. T. Garcia-Esparza, J. W. Lee, G. Kang, S. Shin, S. S. Jeon and H. Lee, *Nanoscale*, 2022, **14**, 9297–9303.
- 151 W. Lou, L. Peng, R. He, Y. Liu and J. Qiao, *J. Colloid Interface Sci.*, 2022, **606**, 994–1003.
- 152 H. Hu, Y. Tang, Q. Hu, P. Wan, L. Dai and X. J. Yang, *Appl. Surf. Sci.*, 2018, **445**, 281–286.
- 153 P. Moreno-García, N. Schlegel, A. Zanetti, A. C. López, M. d. J. Gálvez-Vázquez, A. Dutta, M. Rahaman and P. Broekmann, *ACS Appl. Mater. Interfaces*, 2018, **10**, 31355–31365.
- 154 S. Lamaison, D. Wakerley, D. Montero, G. Rousse, D. Taverna, D. Giaume, D. Mercier, J. Blanchard, H. N. Tran, M. Fontecave and V. Mougél, *ChemSusChem*, 2019, **12**, 511–517.
- 155 J. Christophe, T. Doneux and C. Buess-Herman, *Electrocatalysis*, 2012, **3**, 139–146.
- 156 D. Kim, J. Resasco, Y. Yu, A. M. Asiri and P. Yang, *Nat. Commun.*, 2014, **5**, 4948.
- 157 D. Kim, C. Xie, N. Becknell, Y. Yu, M. Karamad, K. Chan, E. J. Crumlin, J. K. Nørskov and P. Yang, *J. Am. Chem. Soc.*, 2017, **139**, 8329–8336.
- 158 Z. Yin, D. Gao, S. Yao, B. Zhao, F. Cai, L. Lin, P. Tang, P. Zhai, G. Wang, D. Ma and X. Bao, *Nano Energy*, 2016, **27**, 35–43.
- 159 M. Li, J. Wang, P. Li, K. Chang, C. Li, T. Wang, B. Jiang, H. Zhang, H. Liu, Y. Yamauchi, N. Umezawa and J. Ye, *J. Mater. Chem. A*, 2016, **4**, 4776–4782.
- 160 Y. Mun, S. Lee, A. Cho, S. Kim, J. W. Han and J. Lee, *Appl. Catal., B*, 2019, **246**, 82–88.
- 161 V. S. S. Mosali, L. Li, G. Puxty, M. D. Horne, A. M. Bond and J. Zhang, *ChemElectroChem*, 2022, **9**, e202101227.
- 162 P. Bumroongsakulsawat and G. H. Kelsall, *Electrochim. Acta*, 2014, **141**, 216–225.

- 163 N. Han, Y. Wang, J. Deng, J. Zhou, Y. Wu, H. Yang, P. Ding and Y. Li, *J. Mater. Chem. A*, 2019, **7**, 1267–1272.
- 164 X. Lu, D. Y. C. Leung, H. Wang, M. K. H. Leung and J. Xuan, *ChemElectroChem*, 2014, **1**, 836–849.
- 165 T. Yuan, Z. Hu, Y. Zhao, J. Fang, J. Lv, Q. Zhang, Z. Zhuang, L. Gu and S. Hu, *Nano Lett.*, 2020, **20**, 2916–2922.
- 166 W. Ma, S. Xie, X.-G. Zhang, F. Sun, J. Kang, Z. Jiang, Q. Zhang, D.-Y. Wu and Y. Wang, *Nat. Commun.*, 2019, **10**, 892.
- 167 J. He, X. Liu, H. Liu, Z. Zhao, Y. Ding and J. Luo, *J. Catal.*, 2018, **364**, 125–130.
- 168 X. Zheng, P. De Luna, F. P. García de Arquer, B. Zhang, N. Becknell, M. B. Ross, Y. Li, M. N. Banis, Y. Li, M. Liu, O. Voznyy, C. T. Dinh, T. Zhuang, P. Stadler, Y. Cui, X. Du, P. Yang and E. H. Sargent, *Joule*, 2017, **1**, 794–805.
- 169 Q. Li, J. Fu, W. Zhu, Z. Chen, B. Shen, L. Wu, Z. Xi, T. Wang, G. Lu, J.-j. Zhu and S. Sun, *J. Am. Chem. Soc.*, 2017, **139**, 4290–4293.
- 170 H. Xie, S. Chen, F. Ma, J. Liang, Z. Miao, T. Wang, H.-L. Wang, Y. Huang and Q. Li, *ACS Appl. Mater. Interfaces*, 2018, **10**, 36996–37004.
- 171 G. O. Larrazábal, T. Shinagawa, A. J. Martín and J. Pérez-Ramírez, *Nat. Commun.*, 2018, **9**, 1477.
- 172 Y. Zhao, C. Wang and G. G. Wallace, *J. Mater. Chem. A*, 2016, **4**, 10710–10718.
- 173 S. Sarfraz, A. T. Garcia-Esparza, A. Jedidi, L. Cavallo and K. Takanabe, *ACS Catal.*, 2016, **6**, 2842–2851.
- 174 J. Zeng, K. Bejtka, W. Ju, M. Castellino, A. Chiodoni, A. Sacco, M. A. Farkhondehfar, S. Hernández, D. Rentsch, C. Battaglia and C. F. Pirri, *Appl. Catal., B*, 2018, **236**, 475–482.
- 175 S. Rasul, D. H. Anjum, A. Jedidi, Y. Minenkov, L. Cavallo and K. Takanabe, *Angew. Chem., Int. Ed.*, 2015, **54**, 2146–2150.
- 176 A. Jedidi, S. Rasul, D. Masih, L. Cavallo and K. Takanabe, *J. Mater. Chem. A*, 2015, **3**, 19085–19092.
- 177 G. O. Larrazábal, A. J. Martín, S. Mitchell, R. Hauert and J. Pérez-Ramírez, *ACS Catal.*, 2016, **6**, 6265–6274.
- 178 Y. Zhang, Z. Cai, Y. Zhao, X. Wen, W. Xu, Y. Zhong, L. Bai, W. Liu, Y. Zhang, Y. Zhang, Y. Kuang and X. Sun, *Nanoscale Horiz.*, 2019, **4**, 490–494.
- 179 X. Xiao, Y. Xu, X. Lv, J. Xie, J. Liu and C. Yu, *J. Colloid Interface Sci.*, 2019, **545**, 1–7.
- 180 W. Zheng, J. Yang, H. Chen, Y. Hou, Q. Wang, M. Gu, F. He, Y. Xia, Z. Xia, Z. Li, B. Yang, L. Lei, C. Yuan, Q. He, M. Qiu and X. Feng, *Adv. Funct. Mater.*, 2020, **30**, 1907658.
- 181 C. Jiménez, J. García, F. Martínez, R. Camarillo and J. Rincón, *Electrochim. Acta*, 2020, **337**, 135663.
- 182 B. Cho, J. Lee, I. P. Roh, M. H. Lee and T. Yu, *J. Alloys Compd.*, 2022, **911**, 164990.
- 183 J. Zeng, M. R. Fiorentin, M. Fontana, M. Castellino, F. Risplendi, A. Sacco, G. Cicero, M. A. Farkhondehfar, F. Drago and C. F. Pirri, *Appl. Catal., B*, 2022, **306**, 121089.
- 184 H. S. Jeon, J. Timoshenko, F. Scholten, I. Sinev, A. Herzog, F. T. Haase and B. R. Cuenya, *J. Am. Chem. Soc.*, 2019, **141**, 19879–19887.
- 185 Y. Wang, Z. Chen, P. Han, Y. Du, Z. Gu, X. Xu and G. Zheng, *ACS Catal.*, 2018, **8**, 7113–7119.
- 186 S. B. Varandili, J. Huang, E. Oveisi, G. L. De Gregorio, M. Mensi, M. Strach, J. Vavra, C. Gadiyar, A. Bhowmik and R. Buonsanti, *ACS Catal.*, 2019, **9**, 5035–5046.
- 187 C.-J. Chang, S.-C. Lin, H.-C. Chen, J. Wang, K. J. Zheng, Y. Zhu and H. M. Chen, *J. Am. Chem. Soc.*, 2020, **142**, 12119–12132.
- 188 Y. Qiu, H. Zhong, W. Xu, T. Zhang, X. Li and H. Zhang, *J. Mater. Chem. A*, 2019, **7**, 5453–5462.
- 189 G. Shi, Y. Xie, L. Du, X. Fu, X. Chen, W. Xie, T.-B. Lu, M. Yuan and M. Wang, *Angew. Chem., Int. Ed.*, 2022, **61**, e202203569.
- 190 H. Yang, Y. Wu, G. Li, Q. Lin, Q. Hu, Q. Zhang, J. Liu and C. He, *J. Am. Chem. Soc.*, 2019, **141**, 12717–12723.
- 191 G. L. De Gregorio, T. Burdyny, A. Loiudice, P. Iyengar, W. A. Smith and R. Buonsanti, *ACS Catal.*, 2020, **10**, 4854–4862.
- 192 D. Bagchi, J. Raj, A. K. Singh, A. Cherevotan, S. Roy, K. S. Manoj, C. P. Vinod and S. C. Peter, *Adv. Mater.*, 2022, **34**, 2109426.
- 193 M. Watanabe, M. Shibata, A. Katoh, T. Sakata and M. Azuma, *J. Electroanal. Chem. Interfacial Electrochem.*, 1991, **305**, 319–328.
- 194 F. Jia, X. Yu and L. Zhang, *J. Power Sources*, 2014, **252**, 85–89.
- 195 J. Albo, A. Sáez, J. Solla-Gullón, V. Montiel and A. Irabien, *Appl. Catal., B*, 2015, **176–177**, 709–717.
- 196 T.-C. Chou, C.-C. Chang, H.-L. Yu, W.-Y. Yu, C.-L. Dong, J.-J. Velasco-Vélez, C.-H. Chuang, L.-C. Chen, J.-F. Lee, J.-M. Chen and H.-L. Wu, *J. Am. Chem. Soc.*, 2020, **142**, 2857–2867.
- 197 J. Wang, H.-Y. Tan, Y. Zhu, H. Chu and H. M. Chen, *Angew. Chem., Int. Ed.*, 2021, **60**, 17254–17267.
- 198 P.-P. Yang, X.-L. Zhang, F.-Y. Gao, Y.-R. Zheng, Z.-Z. Niu, X. Yu, R. Liu, Z.-Z. Wu, S. Qin, L.-P. Chi, Y. Duan, T. Ma, X.-S. Zheng, J.-F. Zhu, H.-J. Wang, M.-R. Gao and S.-H. Yu, *J. Am. Chem. Soc.*, 2020, **142**, 6400–6408.
- 199 Q. Lei, H. Zhu, K. Song, N. Wei, L. Liu, D. Zhang, J. Yin, X. Dong, K. Yao, N. Wang, X. Li, B. Davaasuren, J. Wang and Y. Han, *J. Am. Chem. Soc.*, 2020, **142**, 4213–4222.
- 200 S. H. Lee, J. C. Lin, M. Farmand, A. T. Landers, J. T. Feaster, E. A. Acosta, J. W. Beeman, Y. Ye, J. Yano, A. Mehta, R. C. Davis, T. F. Jaramillo, C. Hahn and W. S. Drisdell, *J. Am. Chem. Soc.*, 2021, **143**, 588–592.
- 201 Y. Feng, Z. Li, H. Liu, C. Dong, J. Wang, S. A. Kulinich and X. Du, *Langmuir*, 2018, **34**, 13544–13549.
- 202 I. Merino-Garcia, J. Albo, J. Solla-Gullón, V. Montiel and A. Irabien, *J. CO2 Util.*, 2019, **31**, 135–142.
- 203 T. Zhang, Z. Li, J. Zhang and J. Wu, *J. Catal.*, 2020, **387**, 163–169.
- 204 T. T. H. Hoang, S. Verma, S. Ma, T. T. Fister, J. Timoshenko, A. I. Frenkel, P. J. A. Kenis and A. A. Gewirth, *J. Am. Chem. Soc.*, 2018, **140**, 5791–5797.
- 205 C. S. Chen, J. H. Wan and B. S. Yeo, *J. Phys. Chem. C*, 2015, **119**, 26875–26882.



- 206 P.-P. Guo, Z.-H. He, S.-Y. Yang, W. Wang, K. Wang, C.-C. Li, Y.-Y. Wei, Z.-T. Liu and B. Han, *Green Chem.*, 2022, **24**, 1527–1533.
- 207 Y. Chen, Z. Fan, J. Wang, C. Ling, W. Niu, Z. Huang, G. Liu, B. Chen, Z. Lai, X. Liu, B. Li, Y. Zong, L. Gu, J. Wang, X. Wang and H. Zhang, *J. Am. Chem. Soc.*, 2020, **142**, 12760–12766.
- 208 T. Akter, H. Pan and C. J. Barile, *J. Phys. Chem. C*, 2022, **126**, 10045–10052.
- 209 J. Huang, M. Mensi, E. Oveisi, V. Mantella and R. Buonsanti, *J. Am. Chem. Soc.*, 2019, **141**, 2490–2499.
- 210 S. Y. Lee, H. Jung, N.-K. Kim, H.-S. Oh, B. K. Min and Y. J. Hwang, *J. Am. Chem. Soc.*, 2018, **140**, 8681–8689.
- 211 H. Mistry, A. S. Varela, C. S. Bonifacio, I. Zegkinoglou, I. Sinev, Y.-W. Choi, K. Kisslinger, E. A. Stach, J. C. Yang, P. Strasser and B. R. Cuenya, *Nat. Commun.*, 2016, **7**, 12123.
- 212 A. D. Handoko, C. W. Ong, Y. Huang, Z. G. Lee, L. Lin, G. B. Panetti and B. S. Yeo, *J. Phys. Chem. C*, 2016, **120**, 20058–20067.
- 213 B. Zhang, J. Zhang, M. Hua, Q. Wan, Z. Su, X. Tan, L. Liu, F. Zhang, G. Chen, D. Tan, X. Cheng, B. Han, L. Zheng and G. Mo, *J. Am. Chem. Soc.*, 2020, **142**, 13606–13613.
- 214 D. Ren, Y. Deng, A. D. Handoko, C. S. Chen, S. Malkhandi and B. S. Yeo, *ACS Catal.*, 2015, **5**, 2814–2821.
- 215 C. S. Chen, A. D. Handoko, J. H. Wan, L. Ma, D. Ren and B. S. Yeo, *Catal. Sci. Technol.*, 2015, **5**, 161–168.
- 216 Y. Zhou, F. Che, M. Liu, C. Zou, Z. Liang, P. De Luna, H. Yuan, J. Li, Z. Wang, H. Xie, H. Li, P. Chen, E. Bladt, R. Quintero-Bermudez, T.-K. Sham, S. Bals, J. Hofkens, D. Sinton, G. Chen and E. H. Sargent, *Nat. Chem.*, 2018, **10**, 974–980.
- 217 D. Gao, I. Zegkinoglou, N. J. Divins, F. Scholten, I. Sinev, P. Grosse and B. R. Cuenya, *ACS Nano*, 2017, **11**, 4825–4831.
- 218 Y. Gao, Q. Wu, X. Liang, Z. Wang, Z. Zheng, P. Wang, Y. Liu, Y. Dai, M.-H. Whangbo and B. Huang, *Adv. Sci.*, 2020, **7**, 1902820.
- 219 H. Jung, S. Y. Lee, C. W. Lee, M. K. Cho, D. H. Won, C. Kim, H.-S. Oh, B. K. Min and Y. J. Hwang, *J. Am. Chem. Soc.*, 2019, **141**, 4624–4633.
- 220 Z. Yin, C. Yu, Z. Zhao, X. Guo, M. Shen, N. Li, M. Muzzio, J. Li, H. Liu, H. Lin, J. Yin, G. Lu, D. Su and S. Sun, *Nano Lett.*, 2019, **19**, 8658–8663.
- 221 J. Zhang, Z. Liu, H. Guo, H. Lin, H. Wang, X. Liang, H. Hu, Q. Xia, X. Zou and X. Huang, *ACS Appl. Mater. Interfaces*, 2022, **14**, 19388–19396.
- 222 F. Yang, W. Fang, Q. Wang, P. Deng and B. Y. Xia, *ACS Sustainable Chem. Eng.*, 2022, **10**, 4677–4682.
- 223 X. Li, J. Wang, X. Lv, Y. Yang, Y. Xu, Q. Liu and H. B. Wu, *Nano-Micro Lett.*, 2022, **14**, 134.
- 224 H. Wang, E. Matios, C. Wang, J. Luo, X. Lu, X. Hu and W. Li, *Nano Lett.*, 2019, **19**, 3925–3932.
- 225 Z.-Q. Liang, T.-T. Zhuang, A. Seifitokaldani, J. Li, C.-W. Huang, C.-S. Tan, Y. Li, P. De Luna, C. T. Dinh, Y. Hu, Q. Xiao, P.-L. Hsieh, Y. Wang, F. Li, R. Quintero-Bermudez, Y. Zhou, P. Chen, Y. Pang, S.-C. Lo, L.-J. Chen, H. Tan, Z. Xu, S. Zhao, D. Sinton and E. H. Sargent, *Nat. Commun.*, 2018, **9**, 3828.
- 226 J. Han, C. Long, J. Zhang, K. Hou, Y. Yuan, D. Wang, X. Zhang, X. Qiu, Y. Zhu, Y. Zhang, Z. Yang, S. Yan and Z. Tang, *Chem. Sci.*, 2020, **11**, 10698–10704.
- 227 Y. Mi, X. Peng, X. Liu and J. Luo, *ACS Appl. Energy Mater.*, 2018, **1**, 5119–5123.
- 228 C. Choi, S. Kwon, T. Cheng, M. Xu, P. Tieu, C. Lee, J. Cai, H. M. Lee, X. Pan, X. Duan, W. A. Goddard and Y. Huang, *Nat. Catal.*, 2020, **3**, 804–812.
- 229 A. Stalinraja, K. Gopalram, S. Venkatesan, S. M. J. S. Ghosh and T. Selvaraj, *Electrochim. Acta*, 2022, **431**, 141078.
- 230 J. Shan, Y. Shi, H. Li, Z. Chen, C. Sun, Y. Shuai and Z. Wang, *Chem. Eng. J.*, 2022, **433**, 133769.
- 231 Y. C. Li, Z. Wang, T. Yuan, D.-H. Nam, M. Luo, J. Wicks, B. Chen, J. Li, F. Li, F. P. G. de Arquer, Y. Wang, C.-T. Dinh, O. Voznyy, D. Sinton and E. H. Sargent, *J. Am. Chem. Soc.*, 2019, **141**, 8584–8591.
- 232 T. T. H. Hoang, S. Ma, J. I. Gold, P. J. A. Kenis and A. A. Gewirth, *ACS Catal.*, 2017, **7**, 3313–3321.
- 233 S. Ma, M. Sadakiyo, R. Luo, M. Heima, M. Yamauchi and P. J. A. Kenis, *J. Power Sources*, 2016, **301**, 219–228.
- 234 C.-T. Dinh, T. Burdyny, M. G. Kibria, A. Seifitokaldani, C. M. Gabardo, F. P. García de Arquer, A. Kiani, J. P. Edwards, P. De Luna, O. S. Bushuyev, C. Zou, R. Quintero-Bermudez, Y. Pang, D. Sinton and E. H. Sargent, *Science*, 2018, **360**, 783–787.
- 235 W. Liu, P. Zhai, A. Li, B. Wei, K. Si, Y. Wei, X. Wang, G. Zhu, Q. Chen, X. Gu, R. Zhang, W. Zhou and Y. Gong, *Nat. Commun.*, 2022, **13**, 1877.
- 236 W. Ma, S. Xie, T. Liu, Q. Fan, J. Ye, F. Sun, Z. Jiang, Q. Zhang, J. Cheng and Y. Wang, *Nat. Catal.*, 2020, **3**, 478–487.
- 237 T.-T. Zhuang, Z.-Q. Liang, A. Seifitokaldani, Y. Li, P. De Luna, T. Burdyny, F. Che, F. Meng, Y. Min, R. Quintero-Bermudez, C. T. Dinh, Y. Pang, M. Zhong, B. Zhang, J. Li, P.-N. Chen, X.-L. Zheng, H. Liang, W.-N. Ge, B.-J. Ye, D. Sinton, S.-H. Yu and E. H. Sargent, *Nat. Catal.*, 2018, **1**, 421–428.
- 238 P. De Luna, R. Quintero-Bermudez, C.-T. Dinh, M. B. Ross, O. S. Bushuyev, P. Todorović, T. Regier, S. O. Kelley, P. Yang and E. H. Sargent, *Nat. Catal.*, 2018, **1**, 103–110.
- 239 J.-J. Lv, M. Jouny, W. Luc, W. Zhu, J.-J. Zhu and F. Jiao, *Adv. Mater.*, 2018, **30**, 1803111.
- 240 Y. Xu, J. P. Edwards, S. Liu, R. K. Miao, J. E. Huang, C. M. Gabardo, C. P. O'Brien, J. Li, E. H. Sargent and D. Sinton, *ACS Energy Lett.*, 2021, **6**, 809–815.
- 241 F. Li, A. Thevenon, A. Rosas-Hernández, Z. Wang, Y. Li, C. M. Gabardo, A. Ozden, C. T. Dinh, J. Li, Y. Wang, J. P. Edwards, Y. Xu, C. McCallum, L. Tao, Z.-Q. Liang, M. Luo, X. Wang, H. Li, C. P. O'Brien, C.-S. Tan, D.-H. Nam, R. Quintero-Bermudez, T.-T. Zhuang, Y. C. Li, Z. Han, R. D. Britt, D. Sinton, T. Agapie, J. C. Peters and E. H. Sargent, *Nature*, 2020, **577**, 509–513.

- 242 C. M. Gabardo, C. P. O'Brien, J. P. Edwards, C. McCallum, Y. Xu, C.-T. Dinh, J. Li, E. H. Sargent and D. Sinton, *Joule*, 2019, **3**, 2777–2791.
- 243 D. Ren, B. S.-H. Ang and B. S. Yeo, *ACS Catal.*, 2016, **6**, 8239–8247.
- 244 D. Ren, J. Gao, L. Pan, Z. Wang, J. Luo, S. M. Zakeeruddin, A. Hagfeldt and M. Grätzel, *Angew. Chem., Int. Ed.*, 2019, **58**, 15036–15040.
- 245 C.-J. Chang, S.-F. Hung, C.-S. Hsu, H.-C. Chen, S.-C. Lin, Y.-F. Liao and H. M. Chen, *ACS Cent. Sci.*, 2019, **5**, 1998–2009.
- 246 L. Shang, X. Lv, L. Zhong, S. Li and G. Zheng, *Small Methods*, 2022, **6**, 2101334.
- 247 L. R. L. Ting, O. Piqué, S. Y. Lim, M. Tanhaei, F. Calle-Vallejo and B. S. Yeo, *ACS Catal.*, 2020, **10**, 4059–4069.
- 248 S. Shen, X. Peng, L. Song, Y. Qiu, C. Li, L. Zhuo, J. He, J. Ren, X. Liu and J. Luo, *Small*, 2019, **15**, 1902229.
- 249 X. Su, Y. Sun, L. Jin, L. Zhang, Y. Yang, P. Kerns, B. Liu, S. Li and J. He, *Appl. Catal., B*, 2020, **269**, 118800.
- 250 Q. Zhu, X. Sun, D. Yang, J. Ma, X. Kang, L. Zheng, J. Zhang, Z. Wu and B. Han, *Nat. Commun.*, 2019, **10**, 3851.
- 251 D. Chi, H. Yang, Y. Du, T. Lv, G. Sui, H. Wang and J. Lu, *RSC Adv.*, 2014, **4**, 37329–37332.
- 252 Y. Song, R. Peng, D. K. Hensley, P. V. Bonnesen, L. Liang, Z. Wu, H. M. Meyer III, M. Chi, C. Ma, B. G. Sumpter and A. J. Rondinone, *ChemistrySelect*, 2016, **1**, 6055–6061.
- 253 D. Gao, I. Sinev, F. Scholten, R. M. Arán-Ais, N. J. Divins, K. Kvashnina, J. Timoshenko and B. R. Cuenya, *Angew. Chem., Int. Ed.*, 2019, **58**, 17047–17053.
- 254 Y. Zhang, K. Li, M. Chen, J. Wang, J. Liu and Y. Zhang, *ACS Appl. Nano Mater.*, 2020, **3**, 257–263.
- 255 X. Su, Z. Jiang, J. Zhou, H. Liu, D. Zhou, H. Shang, X. Ni, Z. Peng, F. Yang, W. Chen, Z. Qi, D. Wang and Y. Wang, *Nat. Commun.*, 2022, **13**, 1322.
- 256 Y. Baek, H. Song, D. Hong, S. Wang, S. Lee, Y.-C. Joo, G.-D. Lee and J. Oh, *J. Mater. Chem. A*, 2022, **10**, 9393–9401.
- 257 W. Su, L. Ma, Q. Cheng, K. Wen, P. Wang, W. Hu, L. Zou, J. Fang and H. Yang, *J. CO2 Util.*, 2021, **52**, 101698.
- 258 X. Zhang, C. Liu, Y. Zhao, L. Li, Y. Chen, F. Raziq, L. Qiao, S.-X. Guo, C. Wang, G. G. Wallace, A. M. Bond and J. Zhang, *Appl. Catal., B*, 2021, **291**, 120030.
- 259 X. Wang, Z. Wang, F. P. García de Arquer, C.-T. Dinh, A. Ozden, Y. C. Li, D.-H. Nam, J. Li, Y.-S. Liu, J. Wicks, Z. Chen, M. Chi, B. Chen, Y. Wang, J. Tam, J. Y. Howe, A. Proppe, P. Todorović, F. Li, T.-T. Zhuang, C. M. Gabardo, A. R. Kirmani, C. McCallum, S.-F. Hung, Y. Lum, M. Luo, Y. Min, A. Xu, C. P. O'Brien, B. Stephen, B. Sun, A. H. Ip, L. J. Richter, S. O. Kelley, D. Sinton and E. H. Sargent, *Nat. Energy*, 2020, **5**, 478–486.
- 260 Z. Gu, H. Shen, Z. Chen, Y. Yang, C. Yang, Y. Ji, Y. Wang, C. Zhu, J. Liu, J. Li, T.-K. Sham, X. Xu and G. Zheng, *Joule*, 2021, **5**, 429–440.
- 261 F. Li, Y. C. Li, Z. Wang, J. Li, D.-H. Nam, Y. Lum, M. Luo, X. Wang, A. Ozden, S.-F. Hung, B. Chen, Y. Wang, J. Wicks, Y. Xu, Y. Li, C. M. Gabardo, C.-T. Dinh, Y. Wang, T.-T. Zhuang, D. Sinton and E. H. Sargent, *Nat. Catal.*, 2020, **3**, 75–82.
- 262 Y. Lum and J. W. Ager, *Energy Environ. Sci.*, 2018, **11**, 2935–2944.
- 263 C. G. Morales-Guio, E. R. Cave, S. A. Nitopi, J. T. Feaster, L. Wang, K. P. Kuhl, A. Jackson, N. C. Johnson, D. N. Abram, T. Hatsukade, C. Hahn and T. F. Jaramillo, *Nat. Catal.*, 2018, **1**, 764–771.
- 264 D. Zang, Q. Li, G. Dai, M. Zeng, Y. Huang and Y. Wei, *Appl. Catal., B*, 2021, **281**, 119426.
- 265 P. Wang, H. Yang, Y. Xu, X. Huang, J. Wang, M. Zhong, T. Cheng and Q. Shao, *ACS Nano*, 2021, **15**, 1039–1047.
- 266 C. Azenha, C. Mateos-Pedrero, M. Alvarez-Guerra, A. Irabien and A. Mendes, *Chem. Eng. J.*, 2022, **445**, 136575.
- 267 Y. Wang, D. Wang, C. J. Dares, S. L. Marquard, M. V. Sheridan and T. J. Meyer, *Proc. Natl. Acad. Sci. U. S. A.*, 2018, **115**, 278–283.
- 268 K. Zhao, X. Nie, H. Wang, S. Chen, X. Quan, H. Yu, W. Choi, G. Zhang, B. Kim and J. G. Chen, *Nat. Commun.*, 2020, **11**, 2455.
- 269 C. Peng, G. Luo, J. Zhang, M. Chen, Z. Wang, T.-K. Sham, L. Zhang, Y. Li and G. Zheng, *Nat. Commun.*, 2021, **12**, 1580.
- 270 R. A. Geioushy, M. M. Khaled, K. Alhooshani, A. S. Hakeem and A. Rinaldi, *Electrochim. Acta*, 2017, **245**, 456–462.
- 271 A. V. Rayer, E. Reid, A. Kataria, I. Luz, S. J. Thompson, M. Lail, J. Zhou and M. Soukri, *J. CO2 Util.*, 2020, **39**, 101159.
- 272 T. Toyao, Z. Maeno, S. Takakusagi, T. Kamachi, I. Takigawa and K.-i. Shimizu, *ACS Catal.*, 2020, **10**, 2260–2297.
- 273 J. R. Kitchin, *Nat. Catal.*, 2018, **1**, 230–232.
- 274 Y. Sun and S. Dai, *Sci. Adv.*, 2021, **7**, eabg1600.
- 275 H. Liu, L. Syama, L. Zhang, C. Lee, C. Liu, Z. Dai and Q. Yan, *SusMat*, 2021, **1**, 482–505.
- 276 D. Roy, S. C. Mandal and B. Pathak, *J. Phys. Chem. Lett.*, 2022, **13**, 5991–6002.
- 277 S. Nellaiappan, N. K. Katiyar, R. Kumar, A. Parui, K. D. Malviya, K. G. Pradeep, A. K. Singh, S. Sharma, C. S. Tiwary and K. Biswas, *ACS Catal.*, 2020, **10**, 3658–3663.
- 278 S.-X. Guo, C. L. Bentley, M. Kang, A. M. Bond, P. R. Unwin and J. Zhang, *Acc. Chem. Res.*, 2022, 23–34.
- 279 Y. Zhang, S.-X. Guo, X. Zhang, A. M. Bond and J. Zhang, *Nano Today*, 2020, **31**, 100835.
- 280 Z. W. Seh, J. Kibsgaard, C. F. Dickens, I. Chorkendorff, J. K. Nørskov and T. F. Jaramillo, *Science*, 2017, **355**, eaad4998.
- 281 R. Yang, J. Duan, P. Dong, Q. Wen, M. Wu, Y. Liu, Y. Liu, H. Li and T. Zhai, *Angew. Chem., Int. Ed.*, 2022, **61**, e202116706.
- 282 D. Higgins, C. Hahn, C. Xiang, T. F. Jaramillo and A. Z. Weber, *ACS Energy Lett.*, 2019, **4**, 317–324.
- 283 L. Ge, H. Rabiee, M. Li, S. Subramanian, Y. Zheng, J. H. Lee, T. Burdyny and H. Wang, *Chem*, 2022, **8**, 663–692.
- 284 S. Overa, B. H. Ko, Y. Zhao and F. Jiao, *Acc. Chem. Res.*, 2022, **55**, 638–648.